

# Retreat of the Great Escarpment of Madagascar from Geomorphic Analysis and Cosmogenic $^{10}\text{Be}$ Concentrations

Yanyan Wang<sup>1</sup>, Sean Willett<sup>1</sup>, Datian Wu<sup>2</sup>, Negar Haghypour<sup>1</sup>, and Marcus Christl<sup>1</sup>

<sup>1</sup>ETH Zurich

<sup>2</sup>China Geological Survey, Shenyang Center

November 30, 2022

## Abstract

The eastern margin of Madagascar has a prominent relief change from the flat coastal plain to the low-relief high plateau, characterizing a typical great escarpment topography at a passive margin. A quantification of the spatial distribution of erosion rates is necessary to understand the rate of landscape evolution. We present catchment-averaged erosion rates from detrital cosmogenic  $^{10}\text{Be}$  concentrations, systematically covering distinct morphological zones of the escarpment. Erosion rates are differentiated across the escarpment, where the high plateau and the coastal plain are slowly eroding with an average rate of 9.7 m/Ma, and the escarpment basins are eroding faster with an average rate of 16.6 m/Ma. The Alaotra-Ankay Graben related basins have the highest erosion rate with an average rate of 27 m/Ma. The spatial pattern of erosion rates indicates a retreating escarpment landscape. Retreat rates calculated from the  $^{10}\text{Be}$  concentrations are from 182 m/Ma to 1886 m/Ma. The rates of escarpment retreat on Madagascar are consistent with a model of a steady retreat from the coastline since the time of rifting, similar to the Western Ghats escarpment on its conjugate margin of the India Peninsula.

1 **Retreat of the Great Escarpment of Madagascar from Geomorphic Analysis and**  
2 **Cosmogenic  $^{10}\text{Be}$  Concentrations**

3

4 **Y. Wang<sup>1</sup>, S. D. Willett<sup>1</sup>, D. Wu<sup>2</sup>, N. Haghpor<sup>1</sup>, M. Christl<sup>3</sup>**

5 <sup>1</sup>ETH Zurich, Department of Earth Sciences, Sonneggstrasse 5, 8092 Zurich, Switzerland.

6 <sup>2</sup>China Geological Survey, Shengyang Center, Huanghe North Street 280, 110034 Shenyang,  
7 China.

8 <sup>3</sup>ETH Zurich, Department of Physics, Laboratory of Ion Beam Physics, Otto-Stern-Weg 5,  
9 8093 Zurich, Switzerland.

10 Corresponding author: Yanyan Wang ([yanyan.wang@erdw.ethz.ch](mailto:yanyan.wang@erdw.ethz.ch))

11

12 **Key Points:**

- 13 • Presentation of new detrital cosmogenic  $^{10}\text{Be}$  data that systematically covers the great  
14 escarpment of eastern Madagascar.
- 15 • Erosion rates inferred from  $^{10}\text{Be}$  concentrations are 9.7 m/Ma to 27 m/Ma,  
16 systematically vary among distinct morphological zones.
- 17 • Escarpment retreat rates from  $^{10}\text{Be}$  concentrations are 182 m/Ma to 1886 m/Ma,  
18 consistent with evidences for captures and divide migration.

19

20

## 21 **Abstract**

22 The eastern margin of Madagascar has a prominent relief change from the flat coastal plain to  
23 the low-relief high plateau, characterizing a typical great escarpment topography at a passive  
24 margin. A quantification of the spatial distribution of erosion rates is necessary to understand  
25 the rate of landscape evolution. We present catchment-averaged erosion rates from detrital  
26 cosmogenic  $^{10}\text{Be}$  concentrations, systematically covering distinct morphological zones of the  
27 escarpment. Erosion rates are differentiated across the escarpment, where the high plateau  
28 and the coastal plain are slowly eroding with an average rate of 9.7 m/Ma, and the  
29 escarpment basins are eroding faster with an average rate of 16.6 m/Ma. The Alaotra-Ankay  
30 Graben related basins have the highest erosion rate with an average rate of 27 m/Ma. The  
31 spatial pattern of erosion rates indicates a retreating escarpment landscape. Retreat rates  
32 calculated from the  $^{10}\text{Be}$  concentrations are from 182 m/Ma to 1886 m/Ma. The rates of  
33 escarpment retreat on Madagascar are consistent with a model of a steady retreat from the  
34 coastline since the time of rifting, similar to the Western Ghats escarpment on its conjugate  
35 margin of the India Peninsula.

36

## 37 **Plain Language Summary**

38 Eastern Madagascar is characterized by a distinct escarpment with high relief, normally  
39 indicative of high erosion rates. We investigate this by measuring erosion rates using  
40 cosmogenic isotope concentrations in sediment derived from throughout Madagascar. We  
41 calculated erosion rates and related these to distinct geomorphic zones. The pattern of erosion  
42 rates is consistent with inland retreat of the escarpment at about 1 km/Ma. This rate is  
43 consistent with geomorphic evidence and is comparable to the conjugate margin of western  
44 India.

45

## 46 **1 Introduction**

47 Madagascar is one of the world's largest islands, separated from the Africa continent  
48 by the Mozambique Channel (Figure 1a). The main water divide of Madagascar follows the  
49 longitudinal axis of the island and separates drainages of the Indian Ocean from the  
50 Mozambique Channel (Figure 1b), although the topography is strongly asymmetric with  
51 eastward-flowing rivers shorter (<150 km) than westward flowing rivers (>300 km).  
52 Madagascar was at the center of the Gondwana supercontinent and was surrounded by the  
53 ancient Africa continent and the continent of the Seychelles-India (Wit, 2003). The rifting  
54 between Madagascar and Seychelles-India started between 120-92 Ma based on ages of  
55 basaltic intrusions and dikes at the eastern margin of Madagascar (Torsvik et al., 1998;  
56 Melluso et al., 2005). Final separation is dated to the late Cretaceous from volcanic provinces  
57 and the oldest seafloor magnetic anomaly in Indian Ocean, Chron 34 (~84 Ma) (Eagles and  
58 Hoang, 2014), and is limited to being older than the Deccan volcanic province eruption at the  
59 western margin of the India peninsula (~65 Ma) (Collier et al., 2008). Rifting between  
60 Madagascar and Seychelles-India has formed the paired mountain ranges along the coast at  
61 the conjugate margins of eastern Madagascar and western India (Gunnell and Harbor, 2008).

62 Unlike the west margin where the central high plateau gradually flattens into the  
63 coastal plain, the east margin is characterized by an escarpment where the relief abruptly  
64 increases from the flat coastal plain to the high flat plateau, with the water divide sitting at or  
65 near the eastern margin of the highlands. The topography of the conjugate margin of western  
66 India, the Western Ghats, is similar and is well-recognized as a great escarpment (Mandal et

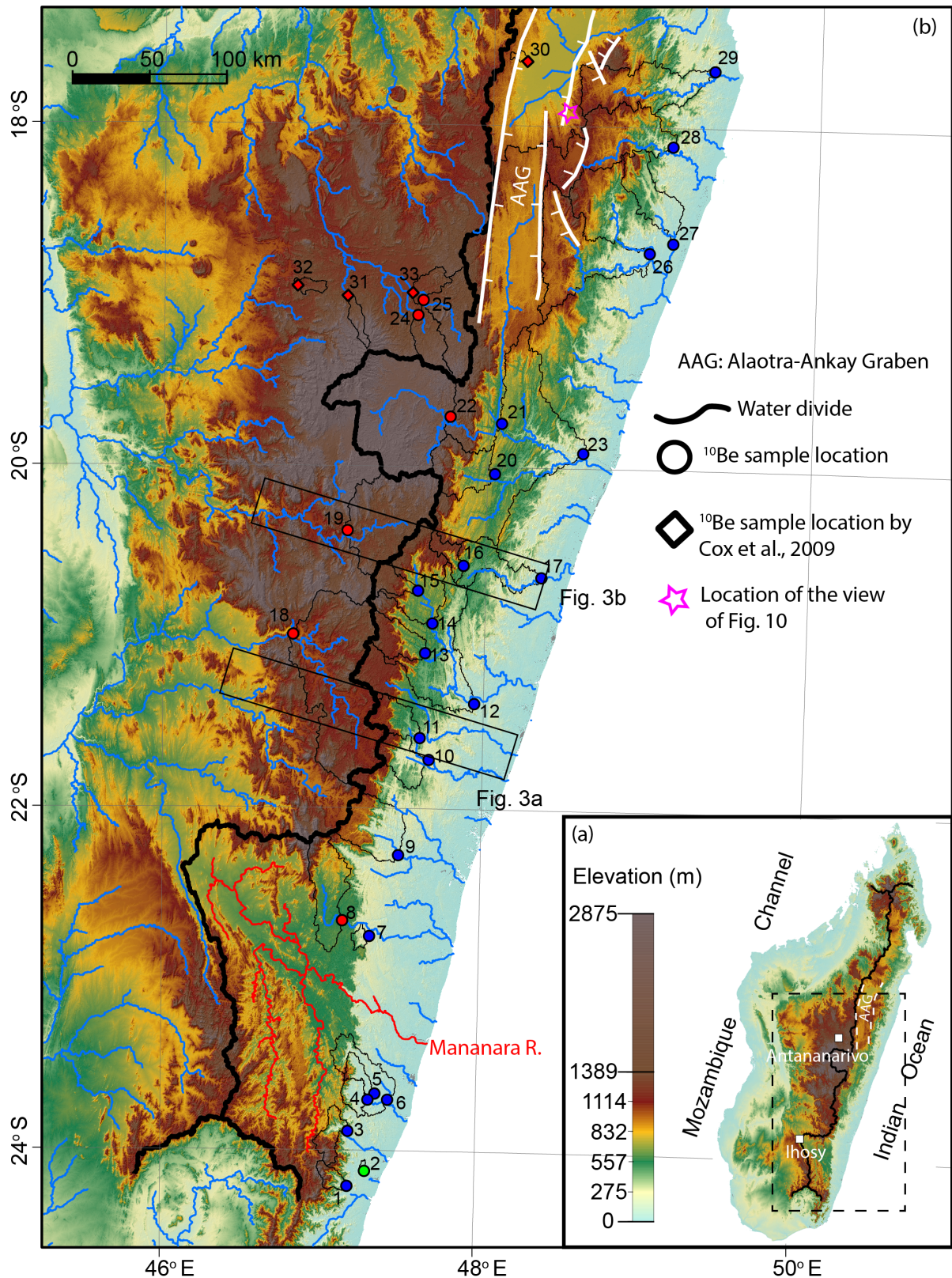
67 al., 2015; Gunnell and Harbor, 2010; Gunnell and Harbor, 2008), but Madagascar has not  
68 received the same attention. In fact, several studies of the Madagascar topography interpret  
69 the high-relief, steep escarpment zone to be river knickpoints formed by recent uplift rather  
70 than rift-related escarpments (Stephenson et al., 2021; Stephenson, 2019; Roberts et al.,  
71 2012).

72 There is some evidence for Cenozoic uplift of Madagascar. A major erosional  
73 unconformity from Oligocene to Miocene (30-16 Ma) is revealed from offshore wells on the  
74 west margin (Delaunay, 2018). This unconformity is likely regional given that Oligocene  
75 sediment is also missing on land (Tucker et al., 2012). Eocene to Pleistocene  
76 marine/shoreface sediment crops out at the western and southern marginal areas (Tucker et  
77 al., 2012; Stephenson et al., 2019) and are currently up to 300 meters above sea level. The  
78 Cenozoic sedimentary rock indicates uplift and westward tilting of Madagascar (Delaunay,  
79 2018). Delaunay (2018) interpreted stepped erosional surfaces on Madagascar as indicating  
80 two major uplift episodes of the central plateau, from the late Cretaceous to early Paleogene  
81 (94-66 Ma) and from the Oligocene to Miocene (34-5Ma).

82 The high central plateau, which defines the western boundary of the escarpment  
83 mountain range, is in a state of isostatic equilibrium, except in the northernmost part of the  
84 island where the relatively high topography can't be purely supported by its crustal thickness  
85 (Andriampenomanana et al., 2017). The northernmost part of Madagascar is characterized by  
86 slow shear-wave velocities in the uppermost mantle (Andriampenomanana et al., 2017; Pratt  
87 et al., 2017). The low shear-wave area coincides with the Neogene to Pleistocene volcanism.  
88 Upwelling, hotter mantle in the northernmost part of Madagascar is interpreted to be  
89 responsible for Pleistocene uplift of the nearby coastal region, where uplifted late  
90 Pleistocene-Holocene coral reefs and marine terrace deposits indicate recent uplift  
91 (Stephenson et al., 2019).

92 Rates of erosion provide important constraints on the landscape evolution. Apatite  
93 fission track ages (AFT) and (U-Th)/He ages on the coastal plain of the eastern margin of  
94 Madagascar are between 68 Ma to 400 Ma (Emmel et al., 2012), rarely significantly younger  
95 than the break-up age, although cooling ages are older on the central high plateau than on the  
96 eastern coastal plain suggesting some effects of rifting (Emmel et al., 2012). However, these  
97 ages are too old and imprecise to distinguish between a retreating escarpment scenario or a  
98 static, or downcutting topography since rifting. Globally, this is typical that  
99 thermochronometry is unable to resolve erosion rates with the precision needed to constrain  
100 landscape evolution models. Short-term erosion rates are slow (~10 m/Ma) on the high  
101 plateau according to sparsely published erosion rates from detrital cosmogenic nuclide  
102 (DCN)  $^{10}\text{Be}$  concentrations (Cox et al., 2009), similar to reported erosion rates for the plateau  
103 hinterland of other passive margins (e.g. the Deccan plateau hinterland of the Western Ghats  
104 (Mandal et al., 2015); the plateau of the southeastern Australia escarpment (Godard et al.,  
105 2019).

106 In this paper, we address the landscape evolution of Madagascar and the formation of  
107 the eastern escarpment through a systematic study of erosion rates determined by detrital  
108 cosmogenic nuclide  $^{10}\text{Be}$  concentrations, with a focus on southeast Madagascar. Regional  
109 patterns of erosion rates and the relationship to the morphology of the landscape are studied.  
110 In particular, we evaluate evidence for the retreat of the escarpment and measure its rate,  
111 making a comparison with the conjugate escarpment of the Western Ghats, India.



112

113 **Figure 1.** (a) The geographic setting of Madagascar. The black dashed box indicates the  
 114 study area. (b) SRTM-90 meter digital elevation model (Jarvis et al., 2008) of Madagascar  
 115 showing the continental water divide, major rivers and cosmogenic nuclide <sup>10</sup>Be basins in this  
 116 research. Rivers with drainage areas larger than 400 km<sup>2</sup> are indicated in blue. The Mananara  
 117 River which we will discuss later is indicated in red. Black polygons are sampled <sup>10</sup>Be

118 catchments.  $^{10}\text{Be}$  sampling locations are shown with circles. Basin type is color-coded: red is  
119 a plateau basin, blue is an escarpment-draining basin and green is a coastal plain basin. White  
120 filled diamonds are  $^{10}\text{Be}$  samples from Cox et al. (2009). Numbers refer to basin ID used in  
121 the main text and associated tables. Thick white lines are simplified normal faults from  
122 Kusky et al. (2010).

123

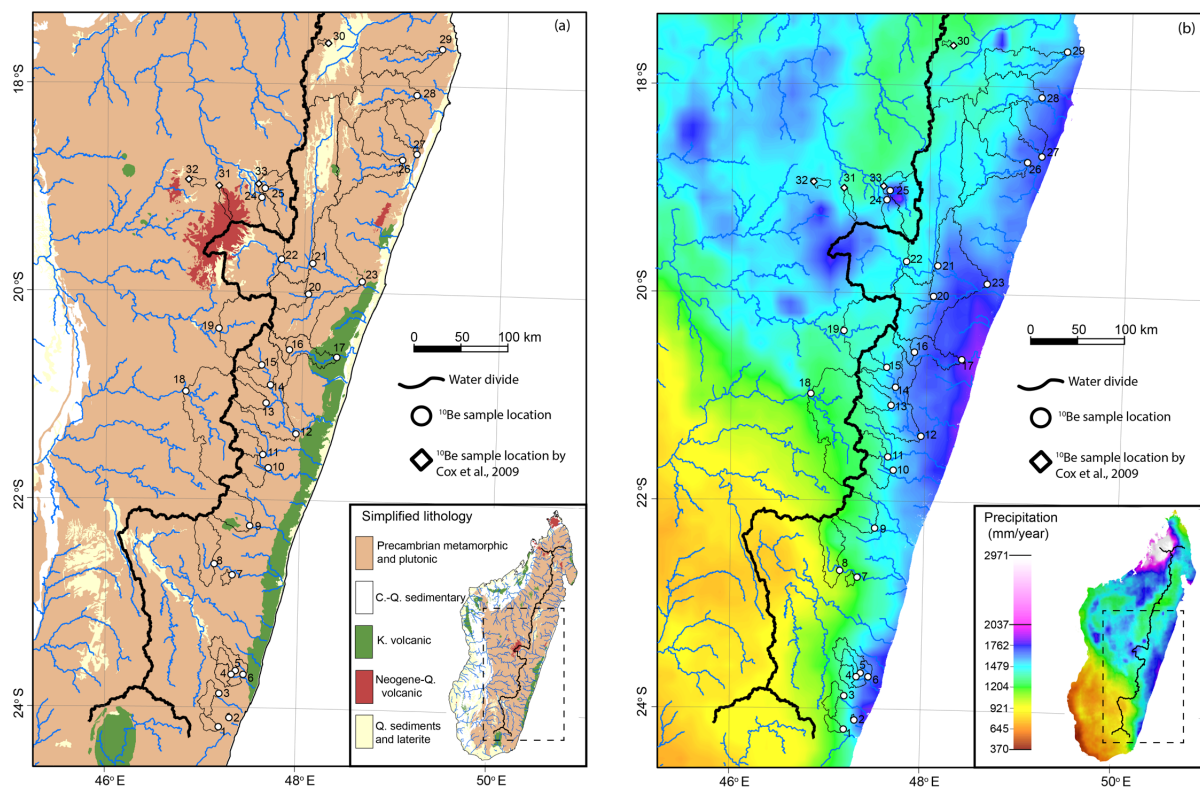
## 124 **2 Study area**

### 125 2.1 Lithology, climate and hydrological setting

126 The geology of Madagascar can be simplified into three domains: the Precambrian  
127 shield of the central and east of the island, rift-related sedimentary sequences from late  
128 Carboniferous to Cretaceous in the west, Cretaceous and Neogene volcanic provinces  
129 distributed across the island (Figure 2a). In our study area, Precambrian paragneiss and  
130 orthogneiss dominate the central plateau, the escarpment, and the coastal plain (Figure 2a).

131 Madagascar is mostly in a tropical climate regime, but the precipitation and  
132 temperature are subject to altitude, monsoon, and proximity to the coastline. The monsoon  
133 moisture comes from the Indian Ocean, impacting mostly southeastern Madagascar (Scroxton  
134 et al., 2017). The annual precipitation decreases from east to west, and also from north to  
135 south (Figure 2b). In the study area, the eastern coastal plain and the escarpment are rainy  
136 year-round, due to an orographic effect (Figure 2a and Figure 3, Ohba et al., 2016). Annual  
137 rainfall in the northern portion of the high plateau is mostly from the summer monsoon  
138 during November to April, whereas the southern part of the central high plateau is subtropical  
139 and dry (Nassor and Jury, 1998). Paleomagnetic studies have reconstructed the paleolatitude  
140 of Madagascar to be between 30°S to 40°S at Chron 34 (~84 Ma) (Schettino and Scotese,  
141 2005). The northward drift of Madagascar pulled it out of subtropical latitudes to the present  
142 tropical zone progressively during the Cenozoic (Ohba et al., 2016).

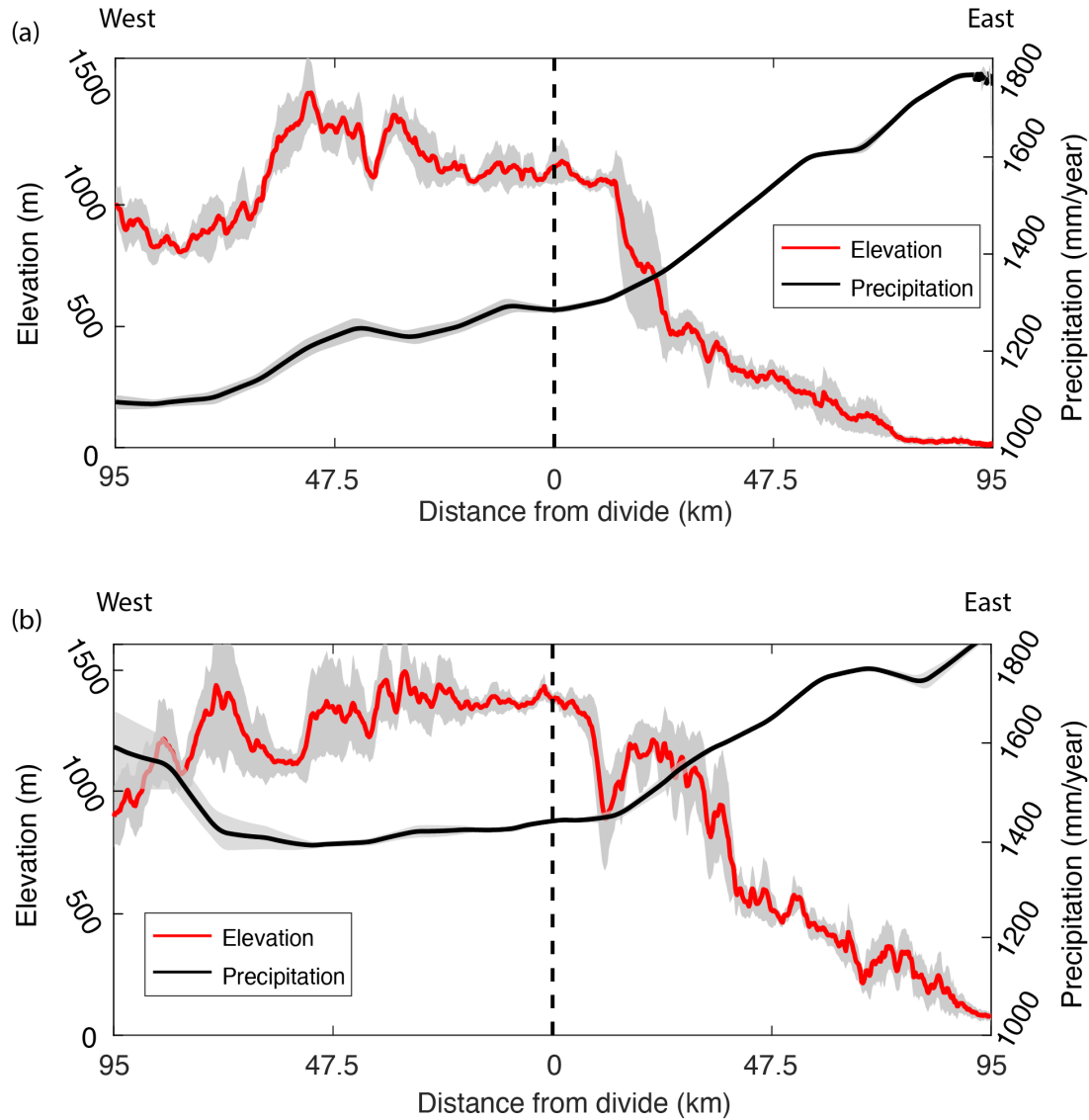
143



144

145 **Figure 2.** (a) Simplified lithology of Madagascar after the geological map from Roig et al.  
 146 (2012) and lithology description from Tucker et al. (2012). (b) Average annual precipitation  
 147 of Madagascar from 2014 to 2018. Raw data is from IMERGHH version 6.0. The IMERGHH  
 148 version 6.0 data were provided by the NASA/Goddard Space Flight Center and PPS, which  
 149 develop and compute the dataset as a contribution to GPM project and archived at the NASA  
 150 GES DISC. Available at: <https://pmm.nasa.gov/data-access/downloads/gpm>.

151



152

153 **Figure 3.** (a) and (b) Swath profiles across the continental water divide showing the  
 154 asymmetric topography and orographic precipitation across the divide. Position of the swaths  
 155 are indicated in Figure 1. Swath window is 30 km wide.

156

## 157 2.2 Morphology

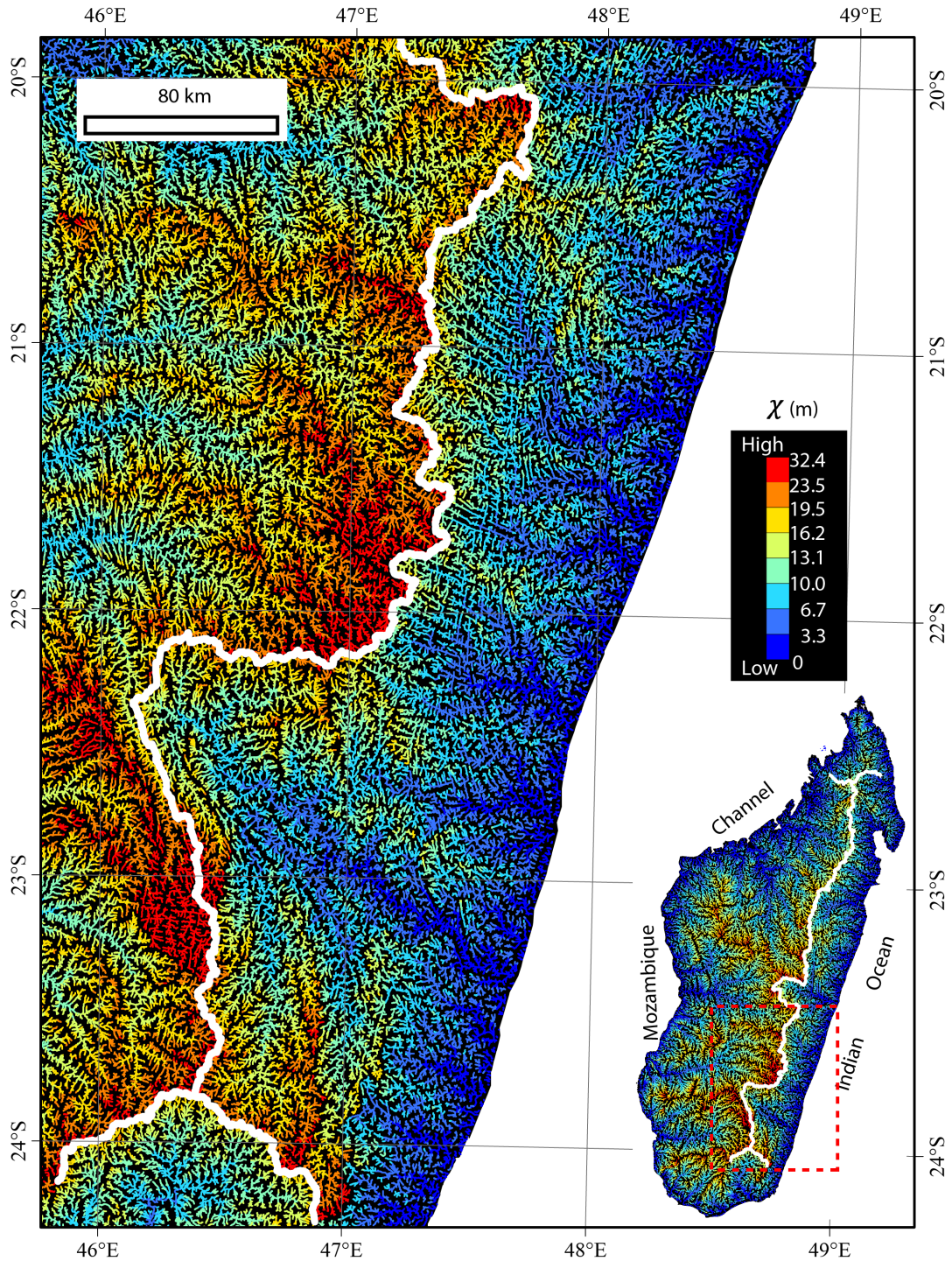
158 Southeastern Madagascar exhibits three topographic domains: the low-lying coastal  
 159 plain on the eastern margin, the highlands of the central plateau, and the high-relief, steep  
 160 escarpment separating the two. Although the escarpment extends for the entire length of the  
 161 island, in the study area, it is most clearly defined for ~500 km in southern Madagascar (Lat.  
 162 19° S-24° S) (Figure 1) where we will focus our study. The coastal plain, escarpment, high  
 163 plateau landscape is also found in other passive margins, e.g. the Western Ghats of India that  
 164 form the conjugate margin to Madagascar (Mandal et al., 2015), the Serra do Mar in southern  
 165 Brazil (Salgado et al., 2016), as well as in the southeastern margin of Australia (Godard et al.,  
 166 2019).

167 The steep and high-relief belt that is located between the low-lying, low-relief coastal  
 168 plain and the low-relief high plateau can be regarded as a passive margin escarpment

169 (Gunnell and Harbor, 2010). A passive margin with a great escarpment is characterized by  
170 rapid elevation gains of hundreds of meters to over one kilometer over a relatively short  
171 distance, forming a prominent asymmetric topography (Matmon et al., 2002). In Madagascar,  
172 the escarpment has a relief of 550-2000 m in the southern Ihosy area and is 1300-2800 m in  
173 the central Antananarivo area (Figure 1). The Madagascar escarpment has similar  
174 morphology to the Western Ghats, a well-recognized great escarpment along the western  
175 margin of the India Peninsula (Gunnell and Harbor, 2008). In Madagascar, north of Lat. 19.5°  
176 S, the active Alaotra-Ankay Graben has affected the morphology of the escarpment (Gunnell  
177 and Harbor, 2008). From Lat. 19.5° S to 24° S, rivers east of the divide frequently follow the  
178 late Proterozoic-gneissic foliations, which are subparallel to the escarpment and brittle  
179 fractures that are oblique to the escarpment (Schreurs et al., 2009). High remnant  
180 escarpments, referred to as “buttes” by Gunnell and Harbor (2010), are prevalent from Lat.  
181 19.5°S to 21.5°S (Figure 1). The coastal plain adjacent to this escarpment segment gently dips  
182 towards the Indian ocean (Figure 3b). The escarpment south of Lat. 21.5°S is lower in  
183 elevation and the buttes are also lower than equivalent features in the northern escarpment  
184 segment (Figure 1).

185         The asymmetry in river length across Madagascar persists after normalization for  
186 drainage area, as indicated by the normalized length parameter,  $\chi$  (Figure 4) (Perron and  
187 Royden, 2013). This asymmetry is likely to be a consequence of the continental rifting which  
188 broke the pre-existing Gondwana-wide continental river network, creating a new base level  
189 for rivers which drain the bordering escarpments. The final rifting on the east coast of  
190 Madagascar set the dominant pattern with a west-migrating continental divide. Other factors  
191 such as climate, lithology and uplift rates can also affect asymmetry. The wetter climate of  
192 the east coast (Nassor and Jury, 1998) should also encourage migration of the divide to the  
193 west. Rivers on the west of the water divide flow across two distinct lithological domains, the  
194 Precambrian crystalline shield and the Mesozoic-Cenozoic sedimentary cover (Figure 2a),  
195 before joining the Mozambique Channel. The sedimentary cover is potentially softer and  
196 more erodible and evidence for this difference is evident in river profiles. Rivers on the east  
197 of the divide carve exclusively into the Precambrian crystalline basement.

198



199

200 **Figure 4.** Systematic  $\chi$  (m) contrast of channel heads across the major water divide (the  
 201 thick white line): high  $\chi$  on west side and low  $\chi$  on east side of the major divide.  $\chi$   
 202 calculation follows Perron and Royden (2013) and includes the mean annual precipitation.  $\chi$   
 203 calculation uses reference drainage of 1 km<sup>2</sup>, reference annual precipitation of 1000 mm/year,  
 204 concavity of 0.45 and base level of sea level.

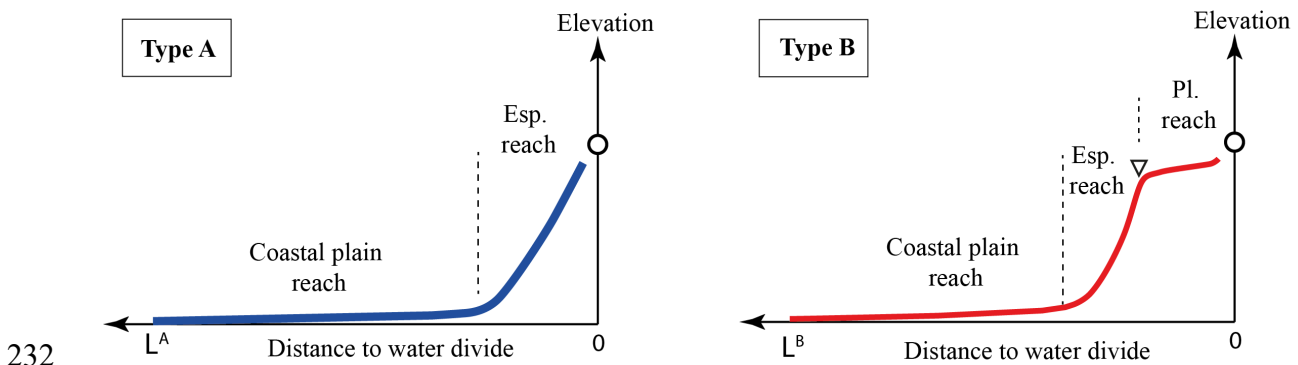
205

206 Escarpment-draining rivers of Madagascar display two distinctive morphologies  
 207 (Figure 5). From the outlet to the water divide, a coastal plain river abruptly steepens at the  
 208 escarpment foot, then flattens again at the top of the escarpment (Type B on Figure 5).

209 Alternatively, many escarpment rivers have no upper low-steepness reach. Instead, these  
 210 retain high steepness until their divide at the top of the escarpment (Type A on Figure 5).  
 211 Both types of escarpment river are segmented in the same way on the transformed  $\chi$ -  
 212 elevation profile.

213 The two distinctive types of escarpment rivers co-exist even within a single  
 214 catchment. In the Namorona River basin, for example, 78% of the major escarpment rivers  
 215 are Type B and 22% are Type A (Figure 6a-c). The escarpment edge is shown as a triangle on  
 216 Figure 6a-c. The escarpment edge appears as a slope-break point on the Type B rivers. The  
 217 conventional view of a suite of knickpoints within a single catchment is that they are a  
 218 consequence of a common, temporal change of uplift. This is testable, either by the common  
 219 elevation to these knickpoints or by plotting the  $\chi$  profiles of all rivers and checking that they  
 220 collapse onto one common profile with co-located knickpoints. The Madagascar escarpment  
 221 rivers do not exhibit common morphologies. The elevation of the knickpoints varies by 500  
 222 meters and they occur over a wide range of  $\chi$  values (Figure 6d). Although spatial variations  
 223 in rock uplift rate or in erodibility can lead to variance in  $\chi$  or elevation, uplift rates in a  
 224 tectonically inactive area will not vary significantly over the short wavelength of a single  
 225 catchment and there are no major lithologic changes within most catchments. Furthermore,  
 226 there is no systematic spatial pattern to the knickpoint  $\chi$  values within a single catchment or  
 227 between catchments. The co-existence of Type A and Type B rivers within a single  
 228 catchment and the high variance in the escarpment edge  $\chi$  and elevation are common across  
 229 Madagascar (Supplement Figure S1-S5), and suggests that it is local, not regional (common  
 230 uplift) processes dictating the morphology of the river profiles.

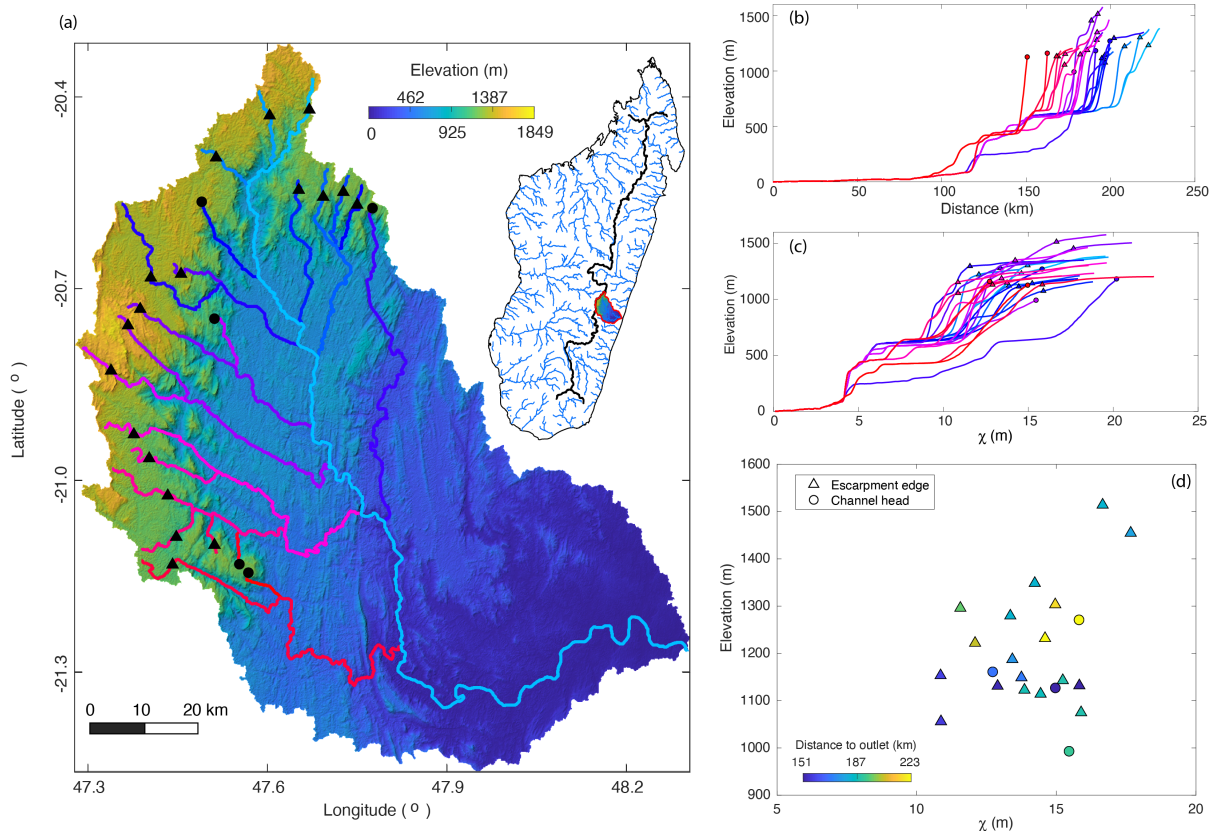
231



232

233 **Figure 5.** Illustration of two distinctive types of river profiles in Madagascar escarpment. The  
 234 circle is the water divide. The triangle indicates the escarpment edge, where this is  
 235 identifiable as a knickzone. Pl. and Esp. are short for plateau and escarpment respectively.

236



237

238 **Figure 6.** (a) SRTM digital elevation model (Jarvis et al., 2008) of an escarpment-draining  
 239 basin, the Namorona River basin in Madagascar. Basin location is indicated in the inset.  
 240 Rivers are extracted from DEM with threshold channel head area of  $1 \text{ km}^2$ . (b) river profiles  
 241 (c) transformed  $\chi$ -elevation profile. (d) Position of the escarpment edge at a channel and  $\chi$   
 242 value of the escarpment edge where this is identifiable as a knickzone or the channel head  
 243 where there is no knickzone.

244

### 245 3 Methodology of interpreting DCN $^{10}\text{Be}$ concentration

246 An important means of determining landscape evolution patterns and rates is by  
 247 establishing rates of surface change. In this study, we present new detrital cosmogenic  
 248 nuclide (DCN) ( $^{10}\text{Be}$ ) concentrations to calculate conventional erosion rates as well as  
 249 applying the recently proposed method for determining escarpment retreat rates directly from  
 250 these data (Wang and Willett, 2021).

251

#### 252 3.1 Sampling strategy and analytical procedures for river sediments

253 We measured catchment-wide erosion rates with *in-situ* produced cosmogenic  $^{10}\text{Be}$   
 254 concentrations from 29 river sand samples. River sand samples were collected from active  
 255 channels in drainage basins on both sides of the continental water divide and cover most of  
 256 the escarpment area (Figure 1). According to the geomorphic features, we divide  $^{10}\text{Be}$  basins  
 257 into three types of catchments (Figure 1). If the outlet is within the central plateau, the basin  
 258 is a plateau basin. If rivers in a basin are fully on the lowland, it is a coastal plain basin.  
 259 Rivers that include the steep escarpment reach and parts of either the plateau or the coastal  
 260 plain are referred to as escarpment rivers. Escarpment rivers can be either type A or B.

261 Escarpment and coastal plain basins are in the tropical rainforest area and are less likely to be  
 262 affected by anthropogenic processes. Plateau basins close to the city of Antananarivo were  
 263 sampled upstream of the city (Sample 24 and 25 on Figure 1). Sampled basins are between  
 264 16 and 17478 km<sup>2</sup> in area.

265 To help assure that samples are representative of the whole catchment, river sediment  
 266 from active channels were amalgamated from samples collected for 200-500 meter along the  
 267 channel. Sediments were sieved into different grain size fractions. Grain size fraction 250-  
 268 500  $\mu\text{m}$  and 125-250  $\mu\text{m}$  was used for quartz purification. Quartz was purified from sieved  
 269 sediments following methods of Lupker et al. (2012): magnetic separation, dissolution in  
 270 mixed H<sub>2</sub>SiF<sub>6</sub> and HCl, then three to five rounds of HF of etchings to remove meteoric Be.  
 271 Be was purified following established protocols by Ochs (1996). Purified quartz was  
 272 dissolved with HF together with  $\sim 0.3$  mg of a commercial carrier solution (Scharlau). Be was  
 273 purified by removal of other elements through cation and anion chromatography. BeOH was  
 274 precipitated and transformed into BeO at 1000°C. Targets for accelerator mass spectrometry  
 275 (AMS) measurements were prepared and <sup>10</sup>Be/<sup>9</sup>Be ratios were measured at the ETH Zurich  
 276 Tandy facility (Christl et al., 2013). The measured <sup>10</sup>Be/<sup>9</sup>Be ratio was normalized to the  
 277 S2007N standard with a nominal <sup>10</sup>Be/<sup>9</sup>Be ratio of  $28.1 (\pm 0.76) \times 10^{-12}$  (Christl et al., 2013)  
 278 which is in accordance with <sup>10</sup>Be half-life  $t_{1/2}$  of  $1.387 (\pm 0.012) \times 10^6$  years (Chmeleff et al.,  
 279 2010). An average <sup>10</sup>Be/<sup>9</sup>Be blank ratio of  $8.1 (\pm 0.70) \times 10^{-15}$  was subtracted from the  
 280 measurements. Uncertainty of blank corrections were also used to correct the uncertainty of  
 281 measurements. After corrections of blank and blank uncertainties, the <sup>10</sup>Be/<sup>9</sup>Be ratio of each  
 282 measurement was converted to <sup>10</sup>Be concentration in atoms per gram of quartz. These  
 283 concentration data are directly used in calculations of erosional mass flux.

284

### 285 3.2 Mass flux calculation

286 Wang and Willett (2021) proposed a method for analysis of detrital cosmogenic  
 287 nuclide concentrations in terms of a directional mass flux. Assuming secular equilibrium of  
 288 cosmogenic nuclide production and export, the measured detrital cosmogenic nuclide  
 289 concentration can be regarded as a ratio between nuclide production and dilution into a  
 290 sediment volume. The volume of sediment is defined by the flux of rock through the Earth's  
 291 surface, but this flux needs not be vertical. Here we use this analysis method to calculate both  
 292 the conventional erosion rate (i.e. vertical mass flux) and the escarpment retreat rate (i.e.  
 293 horizontal mass flux) from <sup>10</sup>Be concentrations. As a general expression,

294

$$|\vec{F}_s| A_{eff} = \frac{\iint_S \Lambda P_0(x, y) dx dy}{\rho C} \quad (1)$$

295

296 Where the  $|\vec{F}_s|$  is the magnitude of the mass flux vector  $\vec{F}_s$ .  $A_{eff}$  is the effective area of the  
 297 catchment surface projected onto a plane normal to the direction of the mass flux: if the mass  
 298 flux  $\vec{F}_s$  is vertical, the effective area  $A_{eff}$  is the basin area as conventionally calculated, for  
 299 example from a DEM; if  $\vec{F}_s$  is horizontal, a projected area for the basin surface onto a  
 300 vertical plane is used in Equation (1).  $\rho$  (gram/cm<sup>3</sup>) is the density of the target,  $\Lambda$  (gram/cm<sup>2</sup>)  
 301 is the free path absorption length,  $P_0(x, y)$  (atoms gram<sup>-1</sup>year<sup>-1</sup>) is the production rate of the  
 302 cosmogenic nuclide at the surface at any given geographic location  $(x, y)$ ,  $S$  is the basin  
 303 surface, and  $C$  (atoms/gram) is the measured concentration of in-situ cosmogenic nuclides. A

304 continuous catchment surface  $S$  can be approximated by discretized elemental surfaces from  
 305 a digital elevation model (DEM). The calculation of the surface integral in Equation (1) is  
 306 approximated by the summation of discretized elemental surfaces  $k$  of the catchment surface:  
 307

$$\iint_S \Lambda P_0(x, y) dx dy = \sum_k \Lambda P_0^k \Delta x \Delta y \quad (2)$$

308

309 where  $P_0^k$  is the production rate of cosmogenic nuclides at the surface for a given elemental  
 310 surface  $k$ . *In situ* cosmogenic  $^{10}\text{Be}$  has three production pathways: neutrons, slow muons and  
 311 fast muons. In practice, the production nuclides from the three pathways are summed together  
 312 to represent the overall cosmogenic production  $P_0^k$  (Lupker et al., 2012):  
 313

$$\Lambda P_0^k = \sum_i \Lambda_i P_{0i}^k \quad (3)$$

314

315 where  $\Lambda_i$  and  $P_{0i}^k$  are the free path absorption length and surface production rate of the  
 316 pathway neutrons, slow muons and fast muons respectively.

317 Equations (1) to (3) are built on the assumption that radioactive decay can be  
 318 neglected, which should be true as long as the condition  $|\vec{F}_s| \rho / \Lambda_i \gg \lambda$  is met (von  
 319 Blanckenburg, 2006) where  $\lambda = \ln 2 / t_{1/2} \approx 1.38 \times 10^{-6} \text{yr}^{-1}$  for  $^{10}\text{Be}$  (Chmeleff et al.,  
 320 2010). The effective attenuation length of neutrons, slow muons and fast muons of  $^{10}\text{Be}$  is  
 321 160, 1500 and 4320  $\text{gram}/\text{cm}^2$  respectively (Braucher et al., 2011). To calculate the surface  
 322 production rates  $P_{0i}^k$  of different pathways, the  $^{10}\text{Be}$  production rate due to neutrons, slow  
 323 muons and fast muons were scaled for latitude and local altitude (Stone, 2000). The sea level  
 324 high latitude (SLHL) production rate of  $3.97(\pm 0.1)$  atoms/gram/yr (Balco et al., 2008) is  
 325 used, following the methodology of Lupker et al. (2012). We did not apply any topographic  
 326 shielding correction (DiBiase, 2018).

327

### 328 3.3 Partition of the erosional mass flux across geomorphic zones

329 Although the continental water divide closely parallels the escarpment edge in  
 330 Madagascar, it coincides with the escarpment edge only about 32% of the time (Figure 1). It  
 331 is unclear if this morphology represents the steady form of the escarpment which is retreating  
 332 while maintaining that form, or if the plateau reach represents a transient feature, for example  
 333 as the remnant of a recent river capture event. If the former is true, the horizontal flux  
 334 calculation would be correct, but if the latter is the case, it is possible that the plateau is  
 335 downcutting in a transient mode that could affect  $^{10}\text{Be}$  concentrations. If the divide is far  
 336 from the escarpment, e.g. basin 13 in Figure 1, the erosional mass flux of this escarpment-  
 337 draining basin could come from both the downcutting of the plateau and the backcutting of  
 338 the escarpment. We can partition the flux between the two as a correction to the purely  
 339 horizontal retreat rate. We assume that a catchment has a high plateau area  $A_p$  with an  
 340 erosion rate of  $e_p$  and that the escarpment is characterized by a mass flux rate of  $v$  through a  
 341 vertical plane with area,  $A_r$ . The overall mass from measured DCN  $^{10}\text{Be}$  concentration  $C$  in  
 342 Equation (1) is a partition of mass between the plateau erosion and the escarpment retreat:  
 343

$$e_p A_p + v A_r = \frac{\iint_S \Delta P_0(x, y) dx dy}{\rho C} \quad (4)$$

344

345 In order to use Equation (4) to correct for the retreat rate  $v$ , the plateau erosion rate  $e_p$   
 346 must be constrained independently, which we do by using the mean erosion rate of plateau  
 347 basins.

348

#### 349 3.4 Correction for flexural uplift on $^{10}\text{Be}$ -inferred retreat rates

350 Isostatic uplift from erosion of the escarpment creates a vertical velocity which, if  
 351 eroded, must also be accounted for in the basin-wide erosional mass. If this isostatic uplift is  
 352 distributed by lithospheric flexure, it will lead to uplift of both the plateau and the coastal  
 353 plain below the escarpment. Uplift of the plateau has no effect on our calculations, but uplift  
 354 of the coastal plain, and the escarpment will affect the mass flux estimate. Assuming that all  
 355 flexural uplift is removed by erosion, the ratio of isostatically-uplifted mass removed relative  
 356 to the retreat mass removal ( $R_A$ ) depends on the lithospheric rigidity and the flexural  
 357 wavelength and can be expressed as (Wang and Willett, 2021):

358

$$R_A = \frac{\rho_{crust}}{2\rho_{mantle}} * \left( \exp\left(-\frac{X_c}{\alpha}\right) \cos\left(\frac{X_c}{\alpha}\right) - 1 \right) \quad (5)$$

359

360 In this expression,  $X_c$  is the distance between the midpoint of the escarpment and the  
 361  $^{10}\text{Be}$  sampling location. Density of the mantle and the crust is given by  $\rho_{mantle}$  and  $\rho_{crust}$   
 362 respectively.  $\alpha$  is the wavelength of isostatic deflection (Turcotte and Schubert, 2002).  
 363 Equation (5) gives the vertical isostatic component of the mass flux as a correction to the  
 364 inferred retreat rate and will be presented with the main results.

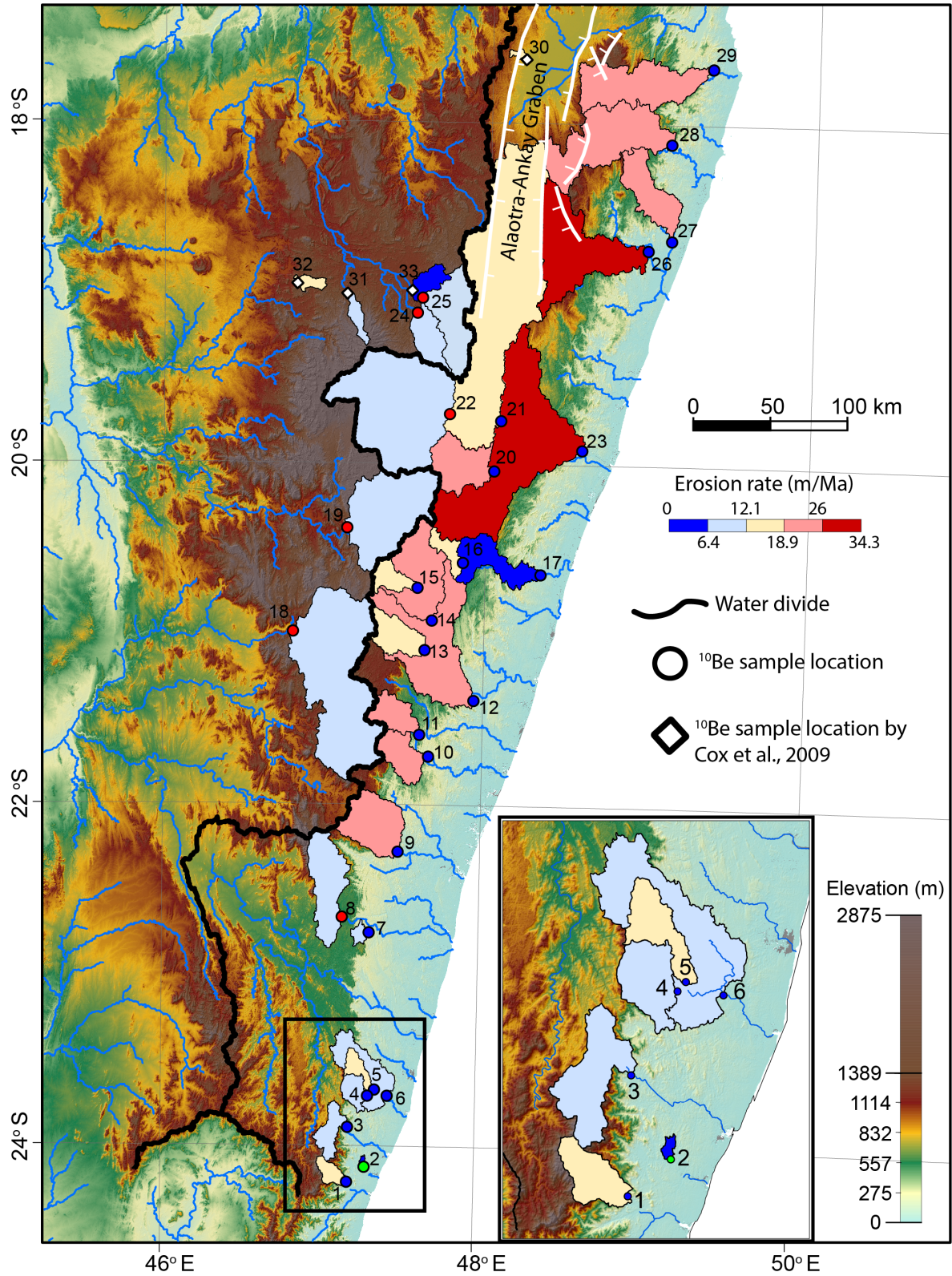
365

## 366 4 Erosion rates of Madagascar: central plateau and east margin

### 367 4.1 Erosion rates of Madagascar

368 We calculated erosion rates from measurement of 29 DCN  $^{10}\text{Be}$  concentrations. DCN  
 369  $^{10}\text{Be}$  concentrations from Cox et al. (2009) are also included, but recalculated according to a  
 370 common protocol. Basins in our area can be divided into two groups: the active graben-  
 371 related basins and the escarpment-related basins, which are further subdivided as discussed  
 372 above in terms of morphology. The highest erosion rates in our study area are found in basins  
 373 affected by graben extension. Erosion rates of the graben-related basins are between 23.1-  
 374 34.3 m/Ma. For the escarpment system, the north-south trending continental water divide and  
 375 the escarpment define four geomorphic zones: the plateau west of the divide, the plateau east  
 376 of the divide, the escarpment, and the lowland plain (Table 1). Erosion rates are generally  
 377 lower on the plateau and on the coastal plain, and are higher if the catchment includes the  
 378 escarpment (Figure 7, Table 1). Erosion rates for plateau basins are between 5.8-12.1 m/Ma.  
 379 Plateau basins (8, 18, 19 and 22) are eroding at similar rates, falling in a narrow range of 7.4-  
 380 10.3 m/Ma. Erosion rates for escarpment basins within Lat. 20° S - 22° S are between 13.1-  
 381 26.0 m/Ma. Escarpment basins in the far south (south of Lat. 22° S) have lower erosion rates

382 of 8.7-14.2 m/Ma. The one basin entirely on the coastal plain has an erosion rate of 6.4  
 383 m/Ma.  
 384



385  
 386 **Figure 7.** Erosion rates of Madagascar from detrital cosmogenic  $^{10}\text{Be}$  concentrations. Erosion  
 387 rates are lower west of the continental water divide, for basins entirely on the plateau, or

388 entirely on the eastern coastal plain. Higher rates are found for the escarpment-draining  
389 catchments and for those associated with the Alaotra-Ankay graben.

390

391 **Table 1.** Summary of  $^{10}\text{Be}$  sample locations, concentrations and erosion rates of Madagascar

Source	Basin	Basin number	Lon. (°)	Lat. (°)	$^{10}\text{Be}$ concentration $\pm 1\sigma$ ( $\times 10^3$ atoms $\text{g}^{-1}$ )		Erosion ( $\text{m}/\text{Ma}$ ) <sup>(b)</sup>			Basin Area ( $\text{km}^2$ )	Surface production rate <sup>(c)</sup> (atoms $\text{g}^{-1} \text{yr}^{-1}$ )		
							Rate	-34%	+34%		$P_n$	$P_{ms}$	$P_{mf}$
Great escarpment system: escarpment basins													
This study	MDG 1653D2	1	47.1890	-24.2261	334.2	13.9	14.2	1.72	1.68	209	6.316	0.018	0.048
This study	MDG 1631B1	3	47.1941	-23.9125	462.6	16.1	10.2	1.21	1.19	407	6.259	0.018	0.048
This study	MDG 1609A1	4	47.3113	-23.7058	281.5	10.0	10.3	1.45	1.42	274	3.549	0.013	0.041
This study	MDG 1586D1	5	47.3339	-23.6822	240.7	7.8	12.9	1.69	1.79	231	3.845	0.014	0.042
This study	MDG 1610A1	6	47.4275	-23.7135	340.6	11.5	8.7	1.20	1.18	1225	3.616	0.013	0.041
This study	MDG 1460C1	7	47.3134	-22.7545	282.5	11.1	10.9	1.50	1.50	108	3.770	0.014	0.042
This study	MDG 1405A1	9	47.4951	-22.2744	144.8	7.7	24.1	3.17	3.41	1262	4.434	0.015	0.044
This study	MDG 1318A2	10	47.6524	-21.7258	136.9	5.7	26.0	3.44	3.42	656	4.512	0.016	0.045
This study	MDG 1287B2	11	47.5869	-21.5768	155.6	8.2	26.0	3.42	3.36	517	5.281	0.017	0.047
This study	MDG 1234D1	12	47.9314	-21.3138	157.8	8.9	25.4	3.21	3.43	4992	5.197	0.017	0.047
This study	MDG 1204C1	13	47.6379	-21.1063	286.2	12.8	16.0	2.00	1.96	690	6.032	0.019	0.049
This study	MDG 1176C1	14	47.6687	-20.9162	201.9	11.3	22.7	2.89	2.92	1863	6.027	0.019	0.049
This study	MDG 1147D1	15	47.5790	-20.7290	294.2	8.1	18.1	2.04	2.01	377	7.143	0.021	0.052
This study	MDG 1122C1	16	47.8701	-20.5835	290.5	11.7	15.7	1.92	1.91	290	5.954	0.019	0.049
This study	MDG1152B1 <sup>(a)</sup>	17	48.3419	-20.6250	959.2	32.8	3.8	0.5	0.5	1189	5.954	0.019	0.049
This study	MDG 1038C1	20	48.0539	-20.0409	224.5	14.7	20.8	2.64	2.84	1091	6.215	0.019	0.049
Great escarpment system: coastal plain basin													
This study	MDG 1654A2	2	47.2928	-24.1229	402.9	12.0	6.4	0.90	0.94	16	3.090	0.012	0.040
Great escarpment system: plateau basins													
This study	MDG 1011B1 <sup>(a)</sup>	22	47.7657	-19.7108	896.8	43.5	7.4	0.87	0.84	4380	7.504	0.020	0.045
This study	MDG 1089D1	19	47.1334	-20.3778	596.5	24.6	10.2	1.17	1.17	2638	8.326	0.023	0.054
This study	MDG 1459B1	8	47.1262	-22.6196	399.4	13.3	10.3	1.25	1.26	1272	5.378	0.017	0.047
This study	MDG 1199B1	18	46.8104	-20.9848	600.7	21.3	8.8	1.03	1.01	4762	7.160	0.021	0.051
this study	MDG Antana2	24	47.5681	-19.0939	607.3	17.5	9.7	1.09	1.07	626	8.066	0.023	0.054
this study	MDG Antana1	25	47.5942	-19.0228	488.6	15.1	12.1	1.35	1.33	1257	8.034	0.023	0.054
Cox et al., 2009	Cox 2004-6A <sup>(a)</sup>	31	47.1251	-19.0045	590.0	18.0	9.7	1.1	1.1	209	8.053	0.023	0.054
Cox et al., 2009	Cox 2004-2A	32	46.8227	-18.9452	370.0	14.0	14.5	1.7	1.7	134	7.260	0.021	0.052
Cox et al., 2009	Cox 2004-9A	33	47.5259	-18.9500	1000.0	23.0	5.8	0.7	0.6	1541	7.977	0.022	0.054
Alaotra-Ankay Graben-related basins													
this study	MDG 1013B1	21	48.0801	-19.7531	288.9	15.4	18.8	2.33	2.33	11508	7.335	0.021	0.052
this study	MDG 1042A1	23	48.5896	-19.9178	141.8	8.6	34.3	4.33	4.45	17478	6.462	0.020	0.050
this study	MDG 0848C1	26	48.9739	-18.7315	113.4	5.5	33.9	4.38	4.43	2624	4.904	0.017	0.046
this study	MDG 0849A2	27	49.1057	-18.6831	132.8	8.6	23.1	3.35	3.48	1051	3.769	0.015	0.043
this study	MDG 0754A2	28	49.1051	-18.1115	157.9	6.7	25.3	3.34	3.05	1679	5.426	0.018	0.048
this study	MDG 0657C1	29	49.3400	-17.6602	153.4	6.5	24.4	3.28	3.19	1936	4.753	0.017	0.046
Cox et al., 2009	Cox 2005-7	30	48.2041	-17.6280	210.0	6.0	18.9	2.3	2.3	56	5.128	0.018	0.048

392 (a) Basaltic surface area is excluded from  $^{10}\text{Be}$  production calculation.

393 (b) The conventional erosion rate is calculated from Equation (1).  $^{10}\text{Be}$  concentrations from  
394 Cox et al. (2009) are recalculated for consistency.

395 (c) Mean basin  $^{10}\text{Be}$  production rates of neutrons ( $P_n$ ), slow muons ( $P_{ms}$ ) and fast muons  
396 ( $P_{mf}$ ). Calculation method follows Lupker et al. (2012).

397

## 398 4.2 Retreat rates of the Madagascar escarpment

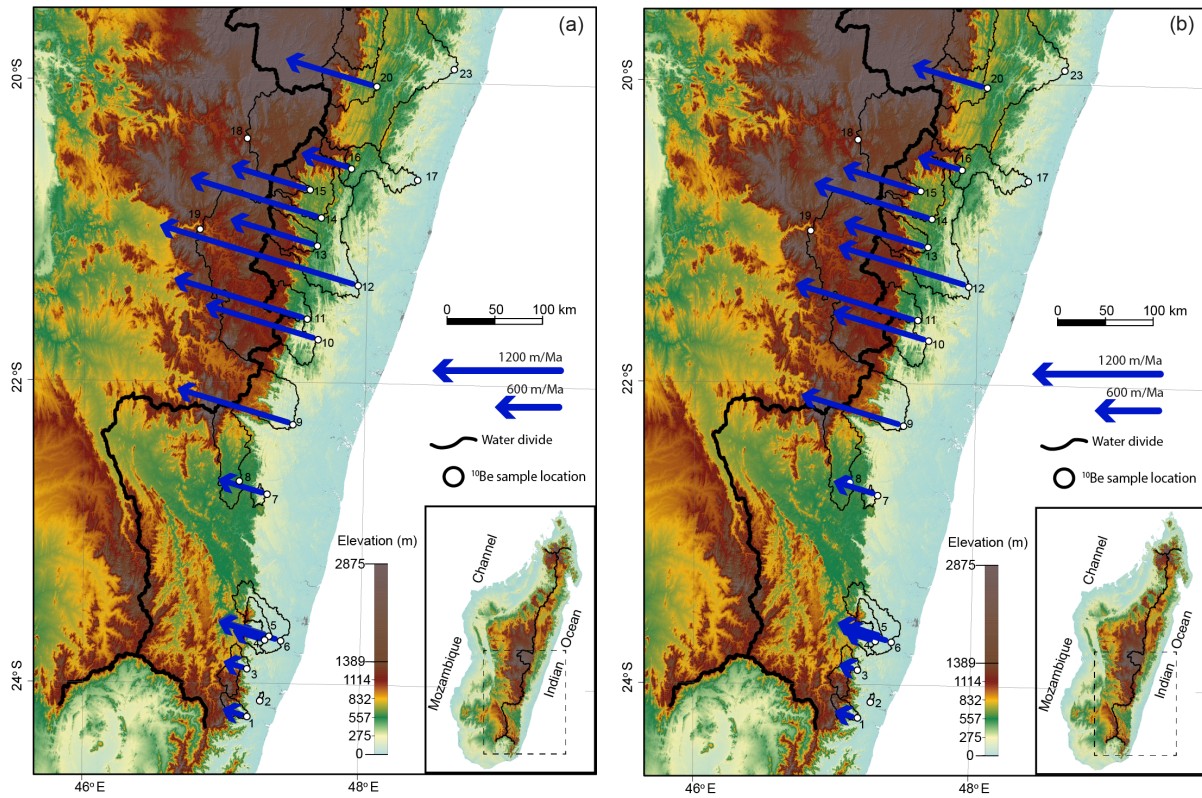
399 Horizontal retreat rates for the escarpment are calculated from the  $^{10}\text{Be}$  concentrations  
400 as in Wang and Willett (2021). Calculation of a horizontal retreat rate requires selection of a  
401 direction. We took a constant direction of N73W, as normal to the coastline and the offshore  
402 continental shelf margin. This direction is used to calculate the projected area  $A_r$  of the  
403 escarpment basin surface. The escarpment is not perfectly parallel to the coast, particularly  
404 where it is influenced by the active Alaotra-Ankay Graben north of Lat.  $20^\circ$  S. South of  $20^\circ$   
405 S, the escarpment segment is morphologically more uniform, so we have focussed our study  
406 here. Retreat rates are between 182-1886 m/Ma (Figure 8a, Table 2). The escarpment  
407 segment that is bounded by escarpment basins 1-7 is retreating slowly at rates of 182-548  
408 m/Ma. The northern segment that is bounded by escarpment basins 9-20 is retreating faster,  
409 at rates of 448-1886 m/Ma. Variations in retreat rates correspond to the distance of the  
410 escarpment to the coastline (Figure 8a), suggesting that the current variations in retreat rate  
411 are representative of the rates over the post-rift time period.

412 As most of our escarpment-draining basins have a significant plateau area, we  
 413 calculated a corrected retreat rate accounting for downward erosion of the plateau area. For  
 414 this correction, we use the erosion rate measured for the four basins that exclusively drain  
 415 from the plateau and have few hillslope collapse features (lavakas) (Plateau Basins 22, 19, 8  
 416 and 18 on Figure 1). The average erosion rate for these basins is 9.17 m/Ma. Corrections for  
 417 plateau area are mostly within the range of  $\pm 10\%$  (Table 2).

418 We also applied the correction for the flexural uplift of the coastal plain and  
 419 escarpment. We calculated corrected retreat rates for different lithospheric rigidities  
 420 (Supplement Table S1). For Table (3) we use a value of 20 km for the effective elastic  
 421 thickness of the lithosphere. These corrections are always downward, and are up to several  
 422 tens of percent of the estimated retreat rate. Corrections are mostly less than 25% (Table 3).

423 Retreat rates after corrections for both plateau area and flexural uplift of the coastal  
 424 plain are smaller than the non-corrected retreat rates but maintain the pattern of spatial  
 425 variability (Figure 8b).

426



427

428 **Figure 8.** Escarpment retreat rates calculated from detrital cosmogenic  $^{10}\text{Be}$  concentrations  
 429 (a) with no correction (b) corrected for plateau area and flexural rebound ( $T_e = 20$  km).  
 430 Arrows represent retreat vectors. The direction is fixed at N73W; vector length represents  
 431 retreat rate (see Table 2 and Table 3 for the data).

432

433

434

435

436 **Table 2.** Escarpment retreat rates for basins of Madagascar

Basin	Distance <sup>(a)</sup> (km)	Retreat rate (m/Ma) no correction			Plateau area (km <sup>2</sup> )	ESP $k_{sn}$ <sup>(c)</sup> (m <sup>0.9</sup> )	Basin $k_{sn}$ <sup>(b)</sup> (m <sup>0.9</sup> )	Retreat rate (m/Ma) corrected for plateau area <sup>(d)</sup>			Correction (%)	Basin number
		Rate	-34%	+34%				Rate	-34%	+34%		
MDG_1653D2	35.6	188.7	22.8	22.2	25	169	142	181.1	23.9	23.9	-4	1
MDG_1631B1	45.1	181.8	21.6	21.2	267	166	97	131.9	31.8	31.3	-27	3
MDG_1609A1	46.1	267.5	37.5	36.7	0	101	33	No need of a correction			4	
MDG_1586D1	45	447.6	58.8	62.1	37	158	57	463	64.5	63.3	3	5
MDG_1610A1	45.5	548.3	75.8	74.8	268	121	34	515.6	80.2	76.6	-6	6
MDG_1460C1	63	425.1	58.4	58.4	20	64	27	411.8	57	60.7	-3	7
MDG_1405A1	72.9	1083	142.3	153.2	445	132	51	1176.5	172.4	183.8	9	9
MDG_1318A2	76.6	1051	139.3	138.3	146	131	54	1062.6	147.5	145.1	1	10
MDG_1287B2	85.5	1247.7	164.3	160.6	235	125	50	1353.5	198.8	202.3	8	11
MDG_1204C1	96.5	802.3	100.5	98.2	367	120	53	896.8	142.6	145.2	12	13
MDG_1147D1	105	718.1	81	79.6	266	142	48	767.7	130.4	121.6	7	15
MDG_1176C1	101.3	1228.6	156.7	158	709	119	47	1351	187.8	202	10	14
MDG_1234D1	99.2	1886	238.5	254.4	1144	111	49	2037.6	282.4	294.5	8	12
MDG_1038C1	96.1	838.2	106.2	114.2	418	121	62	850.6	119.8	118.2	1	20
MDG_1122C1	81.4	441.1	52.6	54.5	153	150	62	416.4	68	67.1	-6	16

437 (a) Distance of the basin-bounded escarpment segment to the coastline. Distance is calculated

438 using a reference retreat direction of N73W.

439 (b) Mean river steepness ( $k_{sn}$ ) of the basin.  $k_{sn}$  is calculated from the integral method440 (topographic gradient in  $\chi$  space (Perron and Royden, 2013)) with precipitation included,  $m/n$   
441 of 0.45 for rivers with threshold drainage 1km<sup>2</sup>.442 (c) Mean river steepness ( $k_{sn}$ ) of the escarpment reach. A threshold of  $k_{sn}=35$  is used to filter  
443 out upper plateau reach and low land reach.444 (d) Correction method follows Equation (4). Madagascar basins are corrected by an average  
445 plateau erosion rate of 9.17 m/Ma.

446

447 **Table 3.** Flexural rebound correction for escarpment retreat rates for basins of Madagascar.

Basin	<sup>(a)</sup> R <sub>A</sub> (%) <sup>(b)</sup> T <sub>e</sub> = 20km)	Retreat rate (m/Ma)							Basin number
		Corrected for flexural only (T <sub>e</sub> = 20 km)			Corrected for both flexure (T <sub>e</sub> = 20 km) and plateau area				
		Rate	-34%	+34%	Rate	-34%	+34%	<sup>(c)</sup> Correction impact (%)	
MDG_1653D2	8.4	173	21	20	166	22	22	-12	1
MDG_1631B1	7.6	168	20	20	122	29	29	-33	3
MDG_1609A1	10.6	239	33	33	239	34	33	-11	4
MDG_1586D1	15.2	380	50	53	393	55	54	-12	5
MDG_1610A1	22.0	428	59	58	402	63	60	-27	6
MDG_1460C1	6.4	398	55	55	385	53	57	-9	7
MDG_1405A1	19.6	871	114	123	946	139	148	-13	9
MDG_1318A2	16.7	875	116	115	885	123	121	-16	10
MDG_1287B2	16.0	1048	138	135	1137	167	170	-9	11
MDG_1204C1	14.8	684	86	84	764	121	124	-5	13
MDG_1147D1	7.1	667	75	74	713	121	113	-1	15
MDG_1176C1	18.2	1005	128	129	1105	154	165	-10	14
MDG_1234D1	40.1	1130	143	152	1221	169	176	-35	12
MDG_1038C1	20.6	666	84	91	675	95	94	-19	20
MDG_1122C1	7.1	410	49	51	387	63	62	-12	16

448 (a) The ratio of isostatically-uplifted mass removed relative to the retreat mass removal in Equation  
449 (5) for a density ratio of 0.85 between the crust and the mantle.

450 (b) Effective elastic thickness of the lithosphere.

451 (c) Compared to the uncorrected retreat rates in Table 2.

452

453 **5 Discussion**454 **5.1 Morphology and rates of landscape change**455 Erosion rates across Madagascar vary systematically with morphology. Our basins  
456 confined to the plateau have an average erosion rate of 9.7 m/Ma, which is similar to other  
457 plateau basins inland of a great escarpment, e.g. the Serra do Mar in southern Brazil (9.2

458 m/Ma) (Salgado et al., 2016), the Deccan Plateau inland of the Western Ghats escarpment of  
459 India (9.6 m/Ma) (Mandal et al., 2015). The average erosion rate for the escarpment basins of  
460 Madagascar is higher, but still low at 16.6 m/Ma. It is among the lowest rates measured for  
461 passive margin escarpments, compared for example to the Western Ghats escarpment (48.6  
462 m/Ma) (Mandal et al., 2015), the southeastern Australian escarpment (32 m/Ma) (Godard et  
463 al., 2019) , the southeastern Brazil escarpment (30.2 m/Ma) (Salgado et al., 2016). However,  
464 this rate does not reflect the erosion rate of the steep escarpment as there are no basins  
465 restricted to the escarpment. Most escarpment basins in our study have a significant portion  
466 of flat plateau. The plateau area represents 12% to 71% of escarpment-draining basins (Table  
467 2). Although difficult to isolate, erosion rates of escarpment basins are substantially higher  
468 than the inland plateau basins, implying differences in erosional processes and efficiency.

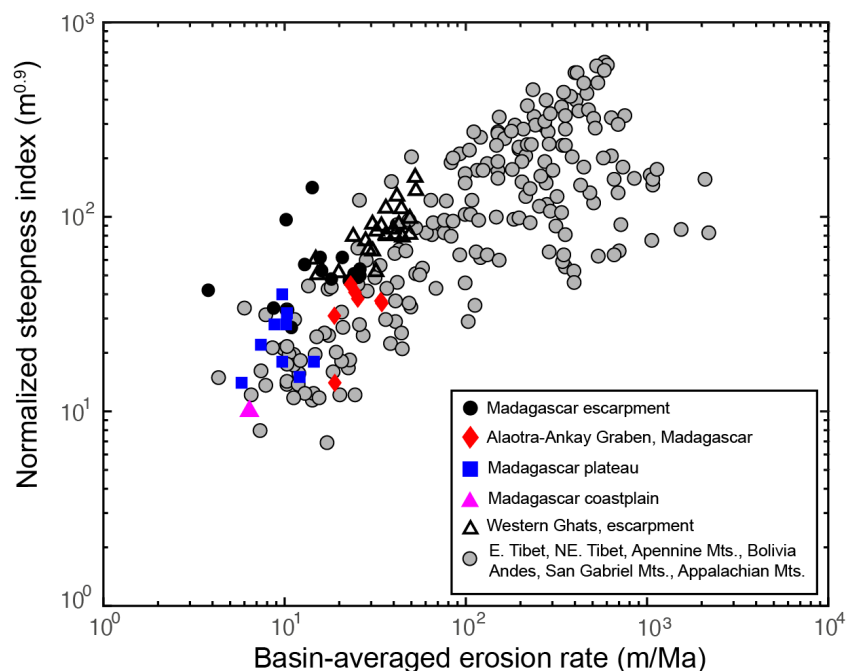
469 Plateau basins are characterized by gentle slopes and deeply weathered saprolite,  
470 implying a lack of fluvial incision even though the precipitation rate is often high. The high  
471 precipitation rate of plateau basins facilitates *in situ* weathering, instead of providing fluvial  
472 incision power, given the low channel slopes. Erosion of the plateau might be limited by  
473 weathering, rather than physical erosion.

474 For their erosion rate, the escarpment basins of Madagascar have some of the highest  
475 river steepness indices measured worldwide (Figure 9). In contrast, the plateau basins, the  
476 coastal plain basin and basins related to the active graben are consistent with more typical  
477 values of river steepness and observed erosion rate. The very high river steepness of  
478 Madagascar escarpment rivers relative to the global empirical relationship of river steepness  
479 and erosion rate supports the model of concentrated erosion at the escarpment and supports  
480 the model of horizontal retreat (Willett et al., 2018).

481 Interpreted as horizontal retreat rates instead of vertical erosion rates gives a very  
482 different view of the landscape dynamics. Escarpment rivers are driving escarpment retreat at  
483 rates of up to 1200 m/Ma (Figure 8). These high rates of retreat explain the steepness of the  
484 escarpment reaches as well as the structure of the river profiles with steep escarpments  
485 contrasting with flat coastal plains and plateaus. Retreat of the water divide into the plateau  
486 and the subsequent, but sporadic, river capture explains the large number of segmented river  
487 profiles and the variability between profiles within single basins. Landscape evolution  
488 dominated by erosion focused onto the escarpment thus provides an explanation for the  
489 morphological observations and the high concentrations of  $^{10}\text{Be}$ , reconciling these seemingly  
490 contradictory observations.

491

492



493

494 **Figure 9.** Normalized channel steepness index and cosmogenic  $^{10}\text{Be}$ -derived basin-averaged  
 495 erosion rate of Madagascar, with comparison to a compilation of global data by Kirby and  
 496 Whipple (2012) (grey colored dots) and Southern Western Ghats (black-lined triangles).

497

498 The basins in the active Alaotra-Ankay Graben display some of the highest vertical  
 499 erosion rates of our study area and are likely to be characterized by vertical erosion. Apart  
 500 from one basin from Cox et al., 2009, which is located on the margin of the Alaotra lake  
 501 (basin 30 on Figure 1), the other basins of this group also comprise a prominent relief zone,  
 502 similar to the regional escarpment (Figure 1). The average erosion rate of the graben basins is  
 503 27 m/Ma, higher than the great escarpment basins although the graben basins are  
 504 characterized by gentler slopes and variable precipitation rates.

505 Active faulting of the graben, coincident with the high rainfall in this area, probably  
 506 triggered the widespread hillslope failure. Intensive, localized hillslope erosion along the  
 507 footwalls of normal faults occurs through gully erosion (Kusky et al., 2010; Voarintsoa et al.,  
 508 2012), a phenomenon that results in formation of geomorphic features referred to as  
 509 “lavakas” in Madagascar (Figure 10). These lavakas develop on thick laterite-saprolite  
 510 mantled hillslopes (Wells et al., 1997; Wells and Andriamihaja, 1990). The collapse of  
 511 hillslopes excavates deeply into the saprolite, exporting a significant amount of highly  
 512 weathered sediment into the rivers. The deep erosion of the hillslope failure in the lavakas  
 513 results in a lower cosmogenic  $^{10}\text{Be}$  concentration compared with normal hillslope colluvium  
 514 sediment (Cox et al., 2009). In places, tens of lavakas can be found per square kilometer (Cox  
 515 et al., 2010). The graben basins in our study area are fed with lavaka sediment and this could  
 516 contribute to the higher erosion rates measured from cosmogenic  $^{10}\text{Be}$  concentrations.

517



518

519 **Figure 10.** Erosional feature known as a lavaka in Madagascar. Location of the photo is  
 520 indicated in Figure 1.

521

## 522 5.2 Comparison between the conjugate margins of Madagascar and India

523 Retreat rates and morphology of the margins of Madagascar and India are compared  
 524 in Figure 11. Lithological differences between the two conjugate margins are likely minimal,  
 525 as both developed on the Precambrian shield and the surface geology is primarily  
 526 metamorphic rock of the shield. The precipitation rate of the Western Ghats escarpment is  
 527 generally larger than the Madagascar escarpment, but is dominated by heavy seasonal  
 528 monsoon rains. Erosion rates of the escarpment-draining basins from Western Ghats are  
 529 higher than the Madagascar escarpment-draining basins (Figure 9). After correction for  
 530 plateau area and flexural compensation, the retreat rates of Western Ghats, however, are  
 531 similar to the Madagascar escarpment (Figure 12). Both margins show the same correlation  
 532 of modern rate with escarpment distance from the coastline.

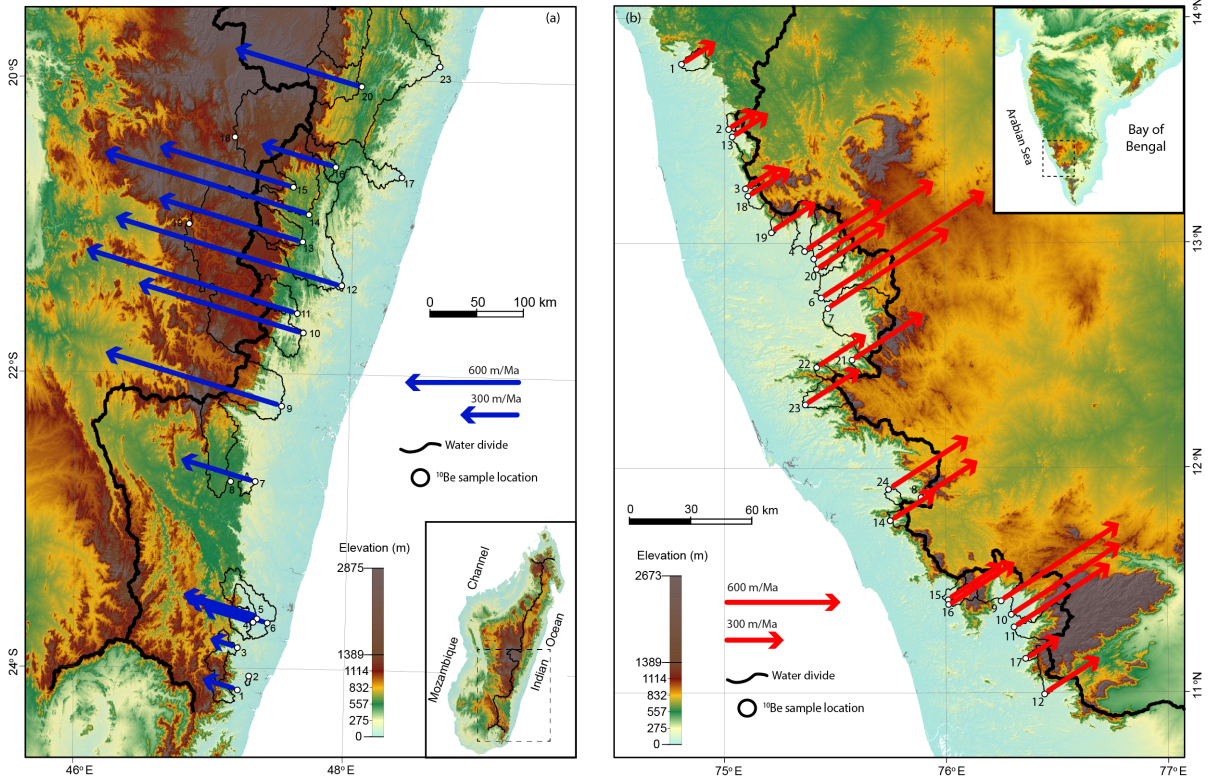
533 The retreat rates we obtain are close to the average retreat rate since rifting (Figure  
 534 12), although our rates are systematically lower, suggesting that rates were faster shortly after  
 535 rifting, or that the timescale of  $^{10}\text{Be}$  accumulation is not capturing the Ma-average properly.  
 536 The discrepancy is also dependent on the age which we take for the onset of escarpment  
 537 retreat. Some constraints are provided for the age of rifting in Figure 12, but escarpment  
 538 retreat would have initiated very early in the rifting process. Once continental rift structures  
 539 were established and rivers were diverted, a mobile divide would form and begin migration.  
 540 We expect that this would have occurred as early as 120 Ma and certainly before 100 Ma, so  
 541 the difference between long-term and  $^{10}\text{Be}$ -based retreat rates might be small.

542 It is also possible that the  $^{10}\text{Be}$  rates are strongly, or systematically, affected by river  
 543 transience given the evidence for discrete capture of rivers from the high plateau. If the  
 544 escarpment is retreating through a series of discrete captures, the basin-averaged erosion rate  
 545 will be cyclic through the process of capture, equilibration and relative stasis prior to the next  
 546 capture. We cannot easily predict the rates or timescale of that cycle, but it is possible that the  
 547 overall bias is downward if the cycle is not symmetric with a long period of stasis leading up  
 548 to the next capture.

549 Confirmational dating of escarpment retreat is difficult to obtain. Dating of laterites  
 550 on the coastal plain can be used as a minimum age for the passage of an escarpment. The  
 551 coastal plain of western India has deep weathering profiles, but most laterite dating has been  
 552 done on the plateau (Beauvais et al., 2016; Bonnet et al., 2014, 2016). An age of 47 Ma was  
 553 obtained from K-Mn oxides in an ore pit that is approximately 10 km away from the

554 escarpment toe of the northern Western Ghats (Beauvais et al., 2016) providing a retreat rate  
 555 of  $\sim 0.2$  km/Ma for the time interval of 47 Ma to the present. This rate is consistent with its  
 556 distance from the coastline. A second age of 27 Ma was obtained nearby, but showed signs of  
 557 secondary weathering, so provided only a minimum age (Beauvais et al., 2016).

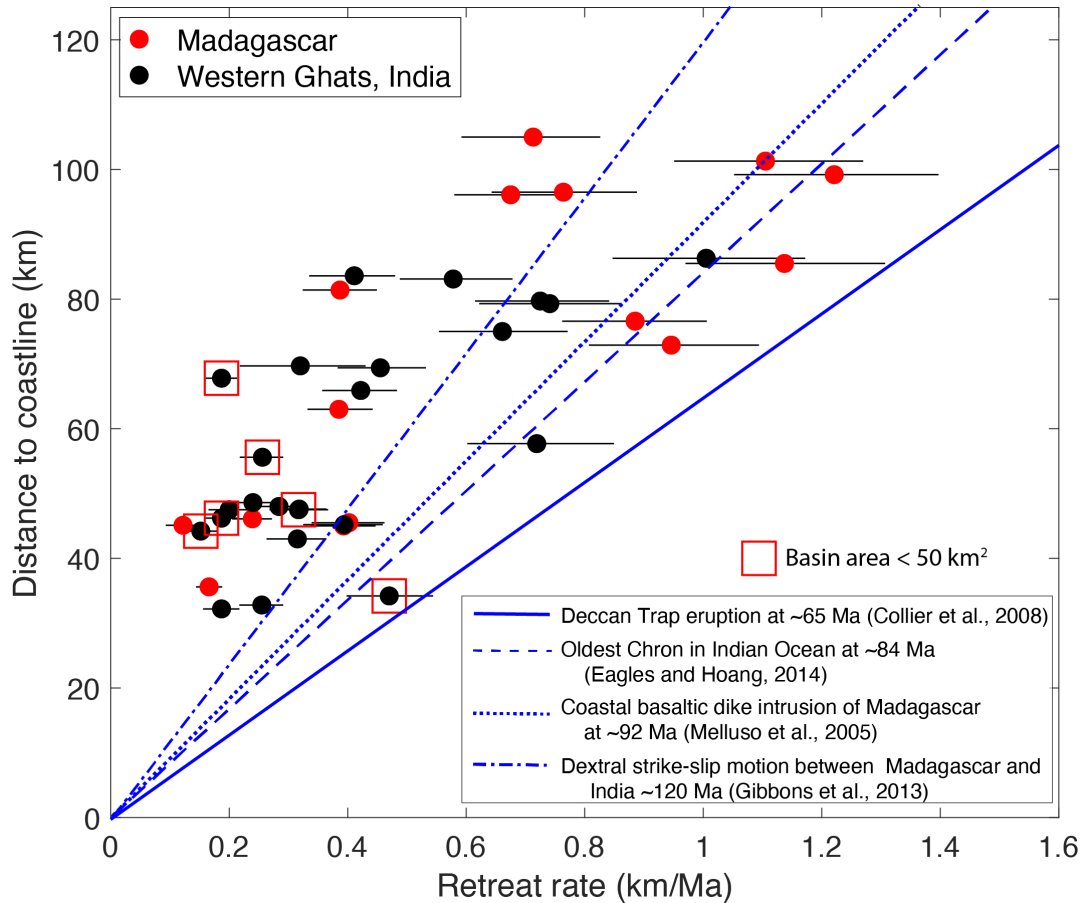
558



559

560 **Figure 11.** Retreat rates of (a) Madagascar (b) Western Ghats, India, calculated with  
 561 identical methodology. All quantities are corrected for plateau area and flexural  
 562 compensation ( $T_e = 20$  km). Continental water divide is shown as thick black lines. Numbers  
 563 nearby  $^{10}\text{Be}$  sample locations on the figure index to respective basins in Table 2-3 and  
 564 Supplement Table S1.

565



566

567 **Figure 12.** Inferred retreat rate of Madagascar escarpment basins from DCN  $^{10}\text{Be}$   
 568 concentrations against current distance from the coastline. Retreat rates of Madagascar  
 569 escarpment are calculated using the Basin Projection method with azimuth taken as N73W.  
 570 Age of rifting is constrained by various events as indicated and is expected to be older than  
 571 these constraints. The retreat rates of Madagascar and Western Ghats are corrected for the  
 572 plateau area from Equation (4) and flexural uplift from Equation (5) for lithosphere elastic  
 573 thickness of 20 km. See Table 3 for the data.

574

### 575 5.3 Escarpment retreat or vertical uplift?

576 The prevalent view of a migrating escarpment is that it represents a water divide,  
 577 perhaps localized by flexural uplift, but migrating inland with the steepest reaches being at or  
 578 near the water divide (Willett et al., 2019; Braun, 2018; Tucker and Slingerland, 1994; Kooi  
 579 and Beaumont, 1994). As an escarpment migrates, it has the potential to capture plateau  
 580 rivers, though the size and frequency of these captures depend on the morphology of the  
 581 plateau river network (Scheingross et al., 2020; Prince et al., 2010). Captures of plateau rivers  
 582 by a Type A escarpment river will form a Type B escarpment river (Giachetta and Willett,  
 583 2018) where the captured plateau river is the low steepness upper reach on a Type B river  
 584 profile. Type B escarpment rivers make up 60% of the escarpment rivers in our study area,  
 585 suggesting that these small-scale capture events are extremely common. Further evidence that  
 586 this morphology is the response of capture includes the low-gradients of the plateau rivers  
 587 and the occurrence of barbed tributaries. River valleys of these plateau-flowing reaches near  
 588 the water divide are typically wide and low-gradient suggesting insufficient sediment

589 transport and erosional power. In addition, low-elevation windgaps are frequent phenomena  
590 at the water divide.

591 It is also possible that the high frequency of type B rivers along the Madagascar  
592 escarpment is due to a nearly continuous migration of this morphology into the plateau. Harel  
593 et al. (2019) demonstrated a mechanism of divide migration by progressive reversal of a  
594 plateau river after capture by an escarpment river. In this model, the water divide and the  
595 escarpment are independent morphologic features, but migrate together and at similar rates.  
596 Upland river capture thus becomes a more continuous process rather than a series of discrete,  
597 transient events. The large frequency of Type B escarpment rivers suggests that this  
598 mechanism might be common in Madagascar. Although Harel et al. (2019) called on easily  
599 eroded alluvium for their model, we expect that the common lateritic surface layer of  
600 Madagascar could serve the same role and its common presence would explain why the water  
601 divide precedes the escarpment so frequently.

602 River captures occur at many scales in Madagascar. For example, the Mananara river  
603 in our study area (Supplement Figure S1), currently drains 1485 km<sup>2</sup> of the highlands to the  
604 east coast. Many of the major tributaries of the Mananara are barbed, flowing to the  
605 northwest for up to 200 kms before reversing to flow to the east over the escarpment and  
606 coastal plain. Schreurs et al. (2009) used this and other evidence to identify this as a major  
607 capture event and we would argue that it follows the Harel et al. (2019) model of a reversed  
608 trunk reach and captured, barbed tributaries, but at a scale of hundreds of kilometers.

609 As an alternative to the migrating escarpment model for Madagascar, a number of  
610 studies have suggested that the modern topography is the result of Cenozoic uplift. Based on  
611 river profile inversion models, Roberts et al. (2012) and Stephenson et al. (2021) proposed  
612 that the high topography of central Madagascar plateau formed in the late Cenozoic from  
613 accelerating uplift initiating between ~15 Ma to ~30 Ma. Based on the identification of  
614 pediment surfaces, Delaunay (2018) proposed that the plateau has undergone episodic uplift  
615 since the Cretaceous with the stepped topography established since the rifting of eastern  
616 Madagascar with Seychelles-India. The cumulative Cenozoic uplift of the Madagascar  
617 plateau is predicted to be 1-2 km from river inversion models (Roberts et al., 2012;  
618 Stephenson et al., 2021) and the pediment surface study of Delaunay (2018). Our escarpment  
619 retreat model suggests that the rate of retreat is consistent with slow retreat since the  
620 Cretaceous rifting, and so, although it does not preclude younger uplift, recent or episodic  
621 uplift is not needed to explain the stepped nature of the east-draining rivers or the kilometer-  
622 scale topography. We would argue that the current morphology and the <sup>10</sup>Be concentrations  
623 are consistent with the major topographic uplift being Cretaceous. The regions of western  
624 Madagascar that were covered in marine sediments have experienced some additional uplift  
625 since deposition, but this need be no more than 1 km to explain the occurrence of marine  
626 sediments at elevation.

627 Vertical uplift and horizontal escarpment retreat into a pre-existing topography  
628 represent alternative models, based on different assumptions. The main difference between  
629 these models is the assumption regarding drainage basin stability. A retreating escarpment  
630 implies continuous divide migration and time-dependent drainage area, whereas river profile  
631 analysis explicitly assumes that drainage area and drainage basin geometry remain constant  
632 in time.

633 We suggest several tests to differentiate between these models of landscape evolution.  
634 First, is the consistency of river profiles. With vertical uplift and a static geometry to river  
635 basin geometry, all river profiles with a common uplift history should exhibit common form  
636 once transformed to  $\chi$ -space (Willett et al., 2014). This is only true for channels with a

637 common uplift history, but in a tectonically inactive area such as Madagascar, rock uplift is  
 638 restricted to long wavelength dynamic topography originating in the mantle. Single  
 639 catchments or neighboring catchments are expected to have a common uplift history. This is  
 640 particularly true for branches of a single catchment where profile variability due to variations  
 641 in uplift rate, rock erodibility or precipitation must originate above the common confluence.  
 642 As shown in Figure 6 and the examples in the supplement (Figure S1-S5) channel profiles  
 643 exhibit large variability, even within single catchments. In many catchments, the large  
 644 knickzones defining the escarpment are present in only a fraction of the channels with a large  
 645 number showing no knickpoint at all (our type A vs. Type B). This is not consistent with the  
 646 idea of a common uplift history, but is consistent with lateral retreat of the escarpment, with  
 647 morphological differences being the result of episodic river capture, as well as transients  
 648 associated with the direction and magnitude of retreat.

649 The second test we can consider is an analysis of the timescale of landscape response  
 650 calibrated to our  $^{10}\text{Be}$  concentration data. Analysis of river steepness or channel profiles,  
 651 including inversion of full channel profiles do not contain any information regarding the  
 652 timescale of transient response. Time information comes through the erodibility parameter,  $K$   
 653 in the stream power model used in these analyses. Cosmogenic concentration data can  
 654 provide an estimate of  $K$  and timescale information.

655 The timescale for a river channel to respond to a baselevel change is (Whipple and  
 656 Tucker, 1999):

657

$$\tau = \frac{1}{K} \int_0^{x^*} \frac{dx}{A(x)^{\frac{m}{n}}} \quad (6)$$

658

659 Where  $\tau$  is referred to as the response time of an uplift signal to propagate upstream from  
 660 baselevel to a position  $x^*$  along the river, and depends on the erodibility,  $K$ , and the  
 661 exponents,  $m$  and  $n$ , of the stream power equation. Defining the basin mean normalized  
 662 steepness index,  $k_{sn}$  (Hilley et al., 2019; Wobus et al., 2006), this can be compared to the  
 663 basin mean erosion rate ( $e$ ) from the  $^{10}\text{Be}$  concentrations to give an estimate of  $K$  through the  
 664 relationship:

665

$$k_{sn} = \left(\frac{e}{K}\right)^{1/n} \quad (7)$$

666

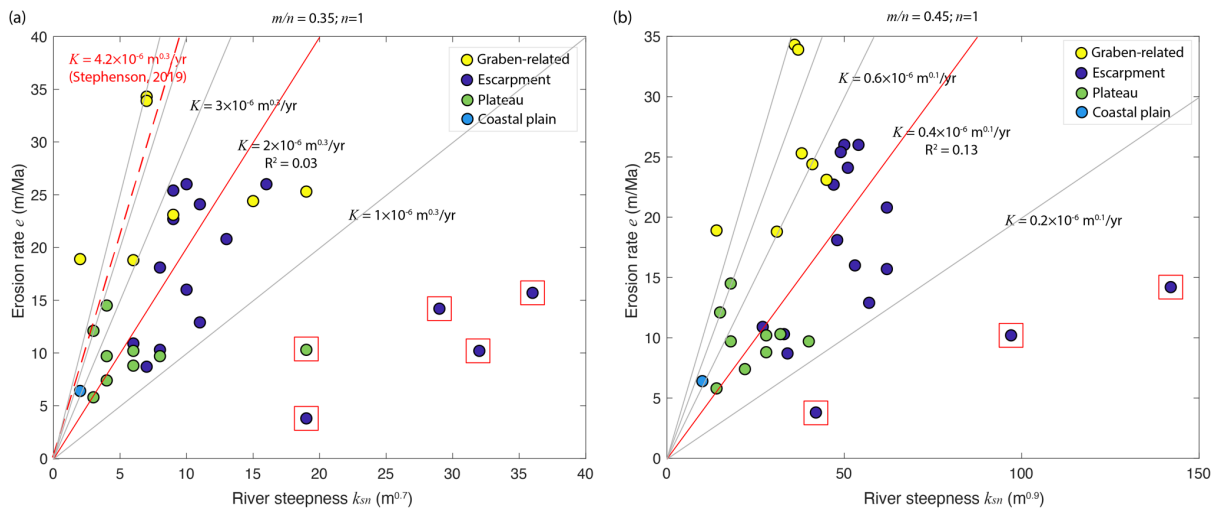
667 Normalized steepness requires an assumption for the ratio of  $m/n$  and Equation (7)  
 668 requires selecting or inferring a value of  $n$ . We assumed  $n=1$  and estimated  $K$  for two values  
 669 of  $m$ . The  $^{10}\text{Be}$  concentrations and the normalized steepness indices are correlated, but not  
 670 well, implying a wide range of erodibility values or strong disequilibrium in channel profiles  
 671 which produces variance in the estimation of basin mean steepness (Figure 13). We find a  
 672 range of  $K$  of  $1.0 \times 10^{-6}$  to  $3.0 \times 10^{-6} \text{m}^{0.3}/\text{yr}$  and  $0.2 \times 10^{-6}$  to  $0.6 \times 10^{-6} \text{m}^{0.1}/\text{yr}$  with  $m=0.35$  and  
 673  $0.45$ , respectively (Figure 13). There are 3 to 5 very low values of  $K$  that might be considered  
 674 outliers (Figure 13). If we ignore the outliers and regress the remaining data with a concavity  
 675 of  $0.45$ , we obtain a  $K$  of  $0.4 \times 10^{-6} \text{m}^{0.1}/\text{yr}$  (Figure 13b), close to the independent estimate of  
 676  $0.24 \times 10^{-6} \text{m}^{0.1}/\text{yr}$  in similar lithology in western India (Mandal et al., 2015). The response  
 677 time for the landscape with these values of  $K$  are shown in Figure 14. Although the range of  
 678 possible timescales is large, the timescales are long relative to the Cenozoic. For many

679 acceptable values of  $K$ , the equilibration timescale is longer than the time since rifting. This  
 680 suggests that in the absence of changes in drainage basin geometry, most of the topography  
 681 would still be unequilibrated to uplift associated with rifting, with no need for Cenozoic  
 682 uplift. Again, this does not preclude Cenozoic uplift, it simply shows that it is not necessary.

683 Stephenson (2019) assumed an  $n=1$ ,  $m=0.35$  and subsequently estimated  $K=4.2\times 10^{-6}$   
 684  $\text{m}^{0.3}/\text{yr}$  based on the elevation of uplifted marine sediments. Roberts et al. (2012) assumed  
 685  $n=1$ ,  $m=0.2$  and calculated  $K=2\times 10^{-4} \text{m}^{0.6}/\text{yr}$  from observations of Miocene marine  
 686 formations that are currently  $\sim 1 \text{ km}$  in elevation. These values of  $K$  are higher than our  
 687 estimate, which greatly reduces the response time of the landscape. The implication is that if  
 688 our  $^{10}\text{Be}$  data correctly characterizes the erosion rates, and the drainage morphology is fixed  
 689 in time, the response time for the landscape would be much longer than the 30 Ma suggested  
 690 by both Roberts et al. (2012), Stephenson (2019) and Stephenson et al. (2021) and  
 691 calibrations to sediment fluxes are offset by a factor of 2 or more.

692 However, although this is a useful exercise to demonstrate the problematic nature of  
 693 fixed basin geometry models and vertical uplift, we do not have much confidence in the  
 694 channel steepness calculations. The transience in river profiles and the intra-basinal variance  
 695 in channel profiles in response to divide migration is too large to make this calculation  
 696 accurately. Nor does it accurately reflect the physical morphology, where the escarpment  
 697 retreat affects concavity which is impossible to differentiate from continuous variation in  
 698 steepness (Willett et al., 2018).

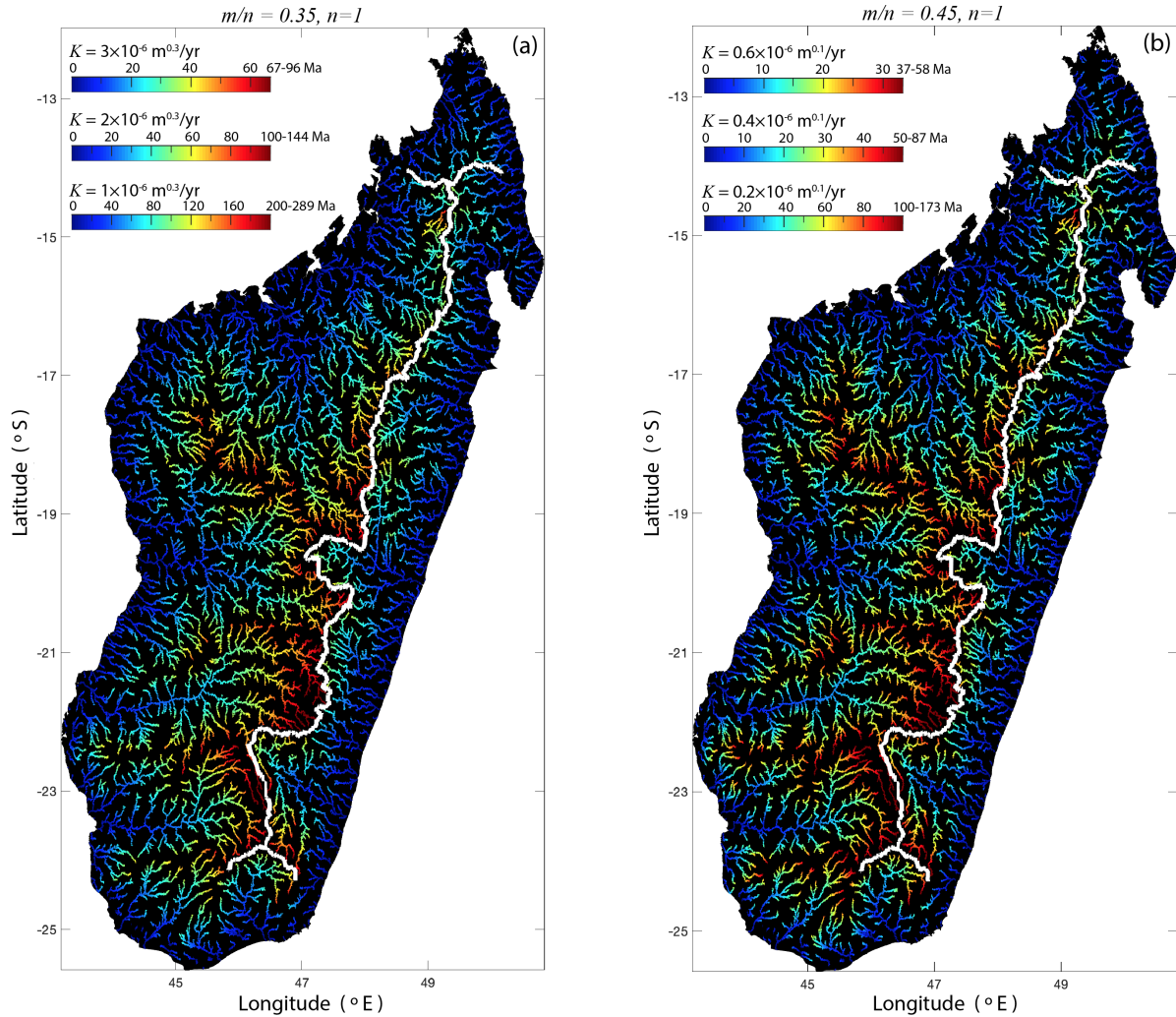
699



700

701 **Figure 13.** Estimate of erodibility constant  $K$  from normalized channel steepness index ( $k_{sn}$ )  
 702 and cosmogenic  $^{10}\text{Be}$ -derived basin-averaged erosion rate ( $e$ ) of Madagascar based on  
 703 Equation (7). The slope exponent  $n=1$ , area exponent (a)  $m=0.35$  and (b)  $m=0.45$ .  
 704 Indeterminate outlier data points are indicated with additional red squares. The red solid lines  
 705 are regressions of data without the outliers. Solid grey lines show values of  $K$  increasing at  
 706 equal intervals that bracket data. The red dashed line shows the  $K$  from Stephenson (2019).

707



708

709 **Figure 14.** Response time  $\tau$  of Madagascar rivers for (a)  $m/n=0.35$  and (b)  $m/n = 0.45$  for  
 710 various  $K$ . Rivers are picked with a drainage area larger than  $64 \text{ km}^2$ . The thick white line  
 711 shows the continental water divide that separates the eastern escarpment drainages and the  
 712 western drainages.

713

## 714 6 Conclusions

715 This study has systematically investigated the erosional fluxes and landscape  
 716 evolution of the Madagascar escarpment. New DCN  $^{10}\text{Be}$  concentration-derived erosion rates  
 717 reveal differential erosion rates among the three geomorphic zones: the erosion rates of the  
 718 plateau and the coastal plain have exceptionally low erosion rates averaging only  $9.7 \text{ m/Ma}$ .  
 719 Erosion rates are higher on the escarpment front and an average erosion rate of  $16.6 \text{ m/Ma}$  is  
 720 calculated for escarpment-draining basins. The active Alaotra-Ankay Graben basins have the  
 721 highest erosion rates in our study area, with an average rate of  $27 \text{ m/Ma}$ .

722 Although the erosion rates are low, the same  $^{10}\text{Be}$  concentrations imply retreat of the  
 723 Madagascar escarpment at rates over an order of magnitude higher. Retreat rates inferred  
 724 from DCN  $^{10}\text{Be}$  concentrations of Madagascar are between  $182 \text{ m/Ma}$ - $1886 \text{ m/Ma}$ . These  
 725 rates are consistent with the distance from the coastline and an average retreat rate since  
 726 rifting. Landscape evolution dominated by escarpment retreat is consistent with the  
 727 asymmetric morphology of Madagascar, geomorphic variance of river profiles and other

728 features characteristic of frequent river capture. We conclude that the landscape evolution of  
 729 Madagascar, and by analogy, the Western Ghats and other passive margin escarpments, are  
 730 dominated by escarpment retreat, drainage basin growth and reorganization and little uplift or  
 731 erosion of pre-existing highlands since rifting.

732

### 733 **References**

- 734 Andriampenanana, F., Nyblade, A. A., Wysession, M. E., Durrheim, R. J., Tilmann, F.,  
 735 Julia, J., . . . others (2017). The structure of the crust and uppermost mantle beneath  
 736 Madagascar. *Geophysical Journal International*, 210 (3), 1525-1544.  
 737 doi:10.1093/gji/ggx243
- 738 Balco, G., Stone, J. O., Lifton, N. A., & Dunai, T. J. (2008). A complete and easily accessible  
 739 means of calculating surface exposure ages or erosion rates from <sup>10</sup>Be and <sup>26</sup>Al  
 740 measurements. *Quaternary geochronology*, 3 (3), 174-195.  
 741 doi:10.1016/j.quageo.2007.12.001
- 742 Beauvais, A., Bonnet, N. J., Chardon, D., Arnaud, N., & Jayananda, M. (2016). Very long-  
 743 term stability of passive margin escarpment constrained by <sup>40</sup>Ar/<sup>39</sup>Ar dating of K-Mn  
 744 oxides. *Geology*, 44 (4), 299-302. doi:10.1130/G37303.1
- 745 Bonnet, N. J., Beauvais, A., Arnaud, N., Chardon, D., & Jayananda, M. (2014). First  
 746 <sup>40</sup>Ar/<sup>39</sup>Ar dating of intense late Palaeogene lateritic weathering in peninsular India.  
 747 *Earth and Planetary Science Letters*, 386 , 126-137. doi:10.1016/j.epsl.2013.11.002
- 748 Bonnet, N. J., Beauvais, A., Arnaud, N., Chardon, D., & Jayananda, M. (2016). Cenozoic  
 749 lateritic weathering and erosion history of peninsular India from <sup>40</sup>Ar/<sup>39</sup>Ar dating of  
 750 supergene K-Mn oxides. *Chemical Geology*, 446 , 33-53.  
 751 doi:10.1016/j.chemgeo.2016.04.018
- 752 Braucher, R., Merchel, S., Borgomano, J., & Bourlès, D. (2011). Production of cosmogenic  
 753 radionuclides at great depth: A multi element approach. *Earth and Planetary Science*  
 754 *Letters*, 309 (1-2), 1-9. doi:10.1016/j.epsl.2011.06.036
- 755 Braun, J. (2018). A review of numerical modeling studies of passive margin escarpments  
 756 leading to a new analytical expression for the rate of escarpment migration velocity.  
 757 *Gondwana Research*, 53 , 209-224. doi:10.1016/j.gr.2017.04.012
- 758 Chmeleff, J., von Blanckenburg, F., Kossert, K., & Jakob, D. (2010). Determination of the  
 759 <sup>10</sup>Be half-life by multicollector ICP-MS and liquid scintillation counting. *Nuclear*  
 760 *Instruments and Methods in Physics Research Section B: Beam Interactions with*  
 761 *Materials and Atoms*, 268 (2), 192-199. doi:10.1016/j.nimb.2009.09.012
- 762 Christl, M., Vockenhuber, C., Kubik, P. W., Wacker, L., Lachner, J., Alifimov, V., & Synal,  
 763 H.-A. (2013). The ETH Zurich AMS facilities: Performance parameters and reference  
 764 materials. *Nuclear Instruments and Methods in Physics Research Section B: Beam*  
 765 *Interactions with Materials and Atoms*, 294 , 29-38. doi:10.1016/j.nimb.2012.03.004
- 766 Collier, J., Sansom, V., Ishizuka, O., Taylor, R., Minshull, T., & Whitmarsh, R. (2008). Age  
 767 of Seychelles-India break-up. *Earth and Planetary Science Letters*, 272 (1-2), 264-  
 768 277. doi:10.1016/j.epsl.2008.04.045
- 769 Cox, R., Bierman, P., Jungers, M. C., & Rakotonirafy, A. M. (2009). Erosion rates and  
 770 sediment sources in Madagascar inferred from <sup>10</sup>Be analysis of lavaka, slope, and  
 771 river sediment. *The Journal of Geology*, 117 (4), 363-376. doi:10.1086/598945

- 772 Cox, R., Zentner, D. B., Rakotondrazafy, A. F. M., & Rasoazanamparany, C. F. (2010).  
 773 Shakedown in Madagascar: Occurrence of lavakas (erosional gullies) associated with  
 774 seismic activity. *Geology*, 38 (2), 179-182. doi:10.1130/G30670.1
- 775 Delaunay, A. (2018). The vertical movements of madagascar (90-0 ma): a coupled analysis  
 776 of the landforms and the dimentional recording of the western Malagasy margins  
 777 (Unpublished doctoral dissertation). Rennes 1.
- 778 DiBiase, R. A. (2018). Increasing vertical attenuation length of cosmogenic nuclide  
 779 production on steep slopes negates topographic shielding corrections for catchment  
 780 erosion rates. *Earth Surface Dynamics*, 6 (4), 923-931. doi: 10.5194/esurf-6-923-2018
- 781 Eagles, G., & Hoang, H. H. (2014). Cretaceous to present kinematics of the Indian, African  
 782 and Seychelles plates. *Geophysical Journal International*, 196 (1), 1-14.  
 783 doi:10.1093/gji/ggt372
- 784 Emmel, B., Boger, S., Jacobs, J., & Daszinnies, M. (2012). Maturity of central Madagascar's  
 785 landscape low-temperature thermochronological constraints. *Gondwana Research*, 21  
 786 (2-3), 704-713. doi:10.1016/j.gr.2011.05.018
- 787 Giachetta, E., & Willett, S. D. (2018). Effects of river capture and sediment flux on the  
 788 evolution of plateaus: insights from numerical modeling and river profile analysis in  
 789 the upper blue Nile catchment. *Journal of Geophysical Research: Earth Surface*, 123  
 790 (6), 1187-1217. doi:10.1029/2017JF004252
- 791 Gibbons, A. D., Whittaker, J. M., & Muller, R. D. (2013). The breakup of east Gondwana:  
 792 Assimilating constraints from cretaceous ocean basins around India into a best-fit  
 793 tectonic model. *Journal of geophysical research: solid earth*, 118 (3), 808-822.  
 794 doi:10.1002/jgrb.50079
- 795 Godard, V., Dosseto, A., Fleury, J., Bellier, O., Siame, L., Team, A., et al. (2019). Transient  
 796 landscape dynamics across the southeastern Australian escarpment. *Earth and  
 797 Planetary Science Letters*, 506 , 397-406. doi:10.1016/j.epsl.2018.11.017
- 798 Gunnell, Y., & Harbor, D. (2008). Structural underprint and tectonic overprint in the Angavo  
 799 (Madagascar) and western ghats (india)-implications for understanding scarp  
 800 evolution at passive margins. *JOURNAL GEOLOGICAL SOCIETY OF INDIA*, 71  
 801 (6), 763. Retrieved from  
 802 <http://www.geosocindia.org/index.php/jgsi/article/view/80750>
- 803 Gunnell, Y., & Harbor, D. (2010). Butte detachment: how pre-rift geological structure and  
 804 drainage integration drive escarpment evolution at rifted continental margins. *Earth  
 805 Surface Processes and Landforms*, 35 (12), 1373-1385. doi:10.1002/esp.1973
- 806 Harel, E., Goren, L., Shelef, E., & Ginat, H. (2019). Drainage reversal toward cliffs induced  
 807 by lateral lithologic differences. *Geology*, 47 (10), 928-932. doi:10.1130/G46353.1
- 808 Hilley, G. E., Porder, S., Aron, F., Baden, C. W., Johnstone, S. A., Liu, F., . . . Young, H. H.  
 809 (2019). Earths topographic relief potentially limited by an upper bound on channel  
 810 steepness. *Nature Geoscience*, 12 (10), 828-832. doi:10.1038/s41561-019-0442-3
- 811 Jarvis, A., Reuter, H., Nelson, A., & Guevara, E. (2008). Hole-filled seamless SRTM data,  
 812 version 4, international centre for tropical agriculture (ciat). Retrieved from  
 813 <http://srtm.csi.cgiar.org>
- 814 Kirby, E., & Whipple, K. X. (2012). Expression of active tectonics in erosional landscapes.  
 815 *Journal of Structural Geology*, 44 , 54-75. doi:10.1016/j.jsg.2012.07.009

- 816 Kooi, H., & Beaumont, C. (1994). Escarpment evolution on high-elevation rifted margins:  
817 Insights derived from a surface processes model that combines diffusion, advection,  
818 and reaction. *Journal of Geophysical Research: Solid Earth*, 99 (B6), 12191-12209.  
819 doi:10.1029/94JB00047
- 820 Kusky, T. M., Toraman, E., Raharimahefa, T., & Rasoazanamparany, C. (2010). Active  
821 tectonics of the Alaotra-Ankay graben system, Madagascar: possible extension of  
822 Somalian-African diffusive plate boundary? *Gondwana Research*, 18 (2-3), 274-294.  
823 doi:10.1016/j.gr.2010.02.003
- 824 Lupker, M., Blard, P.-H., Lave, J., France-Lanord, C., Leanni, L., Puchol, N., . . . Bourles, D.  
825 (2012). 10be-derived himalayan denudation rates and sediment budgets in the ganga  
826 basin. *Earth and Planetary Science Letters*, 333 , 146-156.  
827 doi:10.1016/j.epsl.2012.04.020
- 828 Mandal, S. K., Lupker, M., Burg, J.-P., Valla, P. G., Haghypour, N., & Christl, M. (2015).  
829 Spatial variability of 10be-derived erosion rates across the southern peninsular indian  
830 escarpment: A key to landscape evolution across passive margins. *Earth and Planetary  
831 Science Letters*, 425 , 154-167. doi:10.1016/j.epsl.2015.05.050
- 832 Matmon, A., Bierman, P., & Enzel, Y. (2002). Pattern and tempo of great escarpment  
833 erosion. *Geology*, 30 (12), 1135-1138.  
834 doi:10.1130/00917613(2002)030h1135:PATOGei2.0.CO;2
- 835 Melluso, L., Morra, V., Brotzu, P., Tommasini, S., Renna, M. R., Duncan, R. A., . . .  
836 D'AMELIO, F. (2005). Geochronology and petrogenesis of the Cretaceous  
837 Antampombato-Ambatovy complex and associated dyke swarm, Madagascar. *Journal  
838 of Petrology*, 46 (10), 1963-1996. doi:10.1093/petrology/egi044
- 839 Nassor, A., & Jury, M. (1998). Intra-seasonal climate variability of madagascar. part 1: Mean  
840 summer conditions. *Meteorology and Atmospheric Physics*, 65 (1), 31-41.  
841 doi:10.1007/BF01030267
- 842 Ochs, S. D. I. (1996). The dating of rock surfaces using in situ produced 10ae, 26 al and 36ci,  
843 with examples from antarctica and the swiss alps (Doctoral dissertation, ETH Zurich,  
844 Zurich). doi:10.3929/ethz-a-001772745
- 845 Ohba, M., Samonds, K. E., LaFleur, M., Ali, J. R., & Godfrey, L. R. (2016). Madagascar's  
846 climate at the k/p boundary and its impact on the island's biotic suite.  
847 *Palaeogeography, Palaeoclimatology, Palaeoecology*, 441 , 688-695.  
848 doi:10.1016/j.palaeo.2015.10.028
- 849 Perron, J.T. and Royden, L. (2013), An integral approach to bedrock river profile analysis.  
850 *Earth Surf. Process. Landforms*, 38: 570-576. doi:10.1002/esp.3302
- 851 Pratt, M. J., Wyssession, M. E., Aleqabi, G., Wiens, D. A., Nyblade, A. A., Shore, P., . . .  
852 others (2017). Shear velocity structure of the crust and upper mantle of Madagascar  
853 derived from surface wave tomography. *Earth and Planetary Science Letters*, 458 ,  
854 405-417. doi:10.1016/j.epsl.2016.10.041
- 855 Prince, P. S., Spotila, J. A., & Henika, W. S. (2010). New physical evidence of the role of  
856 stream capture in active retreat of the blue ridge escarpment, southern appalachians.  
857 *Geomorphology*, 123 (3-4), 305-319. doi:10.1016/j.geomorph.2010.07.023
- 858 Roberts, G. G., Paul, J. D., White, N., & Winterbourne, J. (2012). Temporal and spatial  
859 evolution of dynamic support from river profiles: A framework for Madagascar.  
860 *Geochemistry, Geophysics, Geosystems*, 13 (4). doi:10.1029/2012GC004040

- 861 Roig, J., Tucker, R., Delor, C., Peters, S., & Th'e veniaut, H. (2012). Map g'eologique de la r  
 862 e publique de madagascar `a l / 1,000,000 ministe re des mines, program de  
 863 gouvernance des ressources min'e rales. R'e publique de Madagascar, Antananarivo.
- 864 Salgado, A. A., Marent, B. R., Cherem, L. F., Bourles, D., Santos, L. J., Braucher, R., &  
 865 Barreto, H. N. (2014). Denudation and retreat of the serra do mar escarpment in  
 866 southern brazil derived from in situ-produced <sup>10</sup>be concentration in river sediment.  
 867 *Earth Surface Processes and Landforms*, 39 (3), 311-319. doi:10.1002/esp.3448
- 868 Scheingross, J. S., Limaye, A. B., McCoy, S. W., & Whittaker, A. C. (2020). The shaping of  
 869 erosional landscapes by internal dynamics. *Nature Reviews Earth & Environment*, 1-  
 870 16. doi:10.1038/s43017-020-0096-0
- 871 Schettino, A., & Scotese, C. R. (2005). Apparent polar wander paths for the major continents  
 872 (200 ma to the present day): a palaeomagnetic reference frame for global plate  
 873 tectonic reconstructions. *Geophysical Journal International*, 163 (2), 727-759.  
 874 doi:10.1111/j.1365-246X.2005.02638.x
- 875 Schreurs, G., Giese, J., Berger, A., & Gnos, E. (2010). A new perspective on the signi\_cance  
 876 of the ranotsara shear zone in madagascar. *International journal of earth sciences*, 99  
 877 (8), 1827-1847. doi:10.1007/s00531-009-0490-9
- 878 Scroxtton, N., Burns, S. J., McGee, D., Hardt, B., Godfrey, L. R., Ranivoharimanana, L., &  
 879 Faina, P. (2017). Hemispherically in-phase precipitation variability over the last 1700  
 880 years in a madagascar speleothem record. *Quaternary Science Reviews*, 164 , 25-36.  
 881 doi:10.1016/j.quascirev.2017.03.017
- 882 Stephenson, S. (2019). Dynamic topography of madagascar and its surroundings (Doctoral  
 883 dissertation, University of Cambridge). doi:10.17863/CAM.38636
- 884 Stephenson, S. N., White, N., Carter, A., Seward, D., Ball, P., & Klocking, M.(2021).  
 885 Cenozoic dynamic topography of madagascar. *Geochemistry, Geophysics,*  
 886 *Geosystems*, e2020GC009624. doi:10.1029/2020GC009624
- 887 Stephenson, S. N., White, N. J., Li, T., & Robinson, L. F. (2019). Disentangling interglacial  
 888 sea level and global dynamic topography: analysis of Madagascar. *Earth and*  
 889 *Planetary Science Letters*, 519 , 61-69. doi:10.1016/j.epsl.2019.04.029
- 890 Stone, J. O. (2000). Air pressure and cosmogenic isotope production. *Journal of Geophysical*  
 891 *Research: Solid Earth*, 105 (B10), 23753-23759. doi:10.1029/2000JB900181
- 892 Torsvik, T., Tucker, R., Ashwal, L., Eide, E., Rakotosolof, N., & De Wit, M. (1998). Late  
 893 cretaceous magmatism in madagascar: palaeomagnetic evidence for a stationary  
 894 marion hotspot. *Earth and Planetary Science Letters*, 164 (1-2), 221-232.  
 895 doi:10.1016/S0012-821X(98)00206-4
- 896 Tucker, G. E., & Slingerland, R. L. (1994). Erosional dynamics, flexural isostasy, and long-  
 897 lived escarpments: A numerical modeling study. *Journal of Geophysical Research:*  
 898 *Solid Earth*, 99 (B6), 12229-12243. doi:10.1029/94JB00320
- 899 Turcotte, D., & Schubert, G. (2002). *Geodynamics*, chapter 3: Elasticity and Cambridge  
 900 University Press. doi:10.1017/CBO9780511807442.005
- 901 Voarintsoa, N., Cox, R., Razanatsheno, M., & Rakotondrazafy, A. (2012). Relation between  
 902 bedrock geology, topography and lavaka distribution in Madagascar. *South African*  
 903 *Journal of Geology*, 115 (2), 225-250. doi:10.2113/gssajg.115.225

- 904 Von Blanckenburg, F. (2005). The control mechanisms of erosion and weathering at basin  
 905 scale from cosmogenic nuclides in river sediment. *Earth and Planetary Science*  
 906 *Letters*, 237 (3-4), 462-479. doi:10.1016/j.epsl.2005.06.030
- 907 Wang, Y., & Willett, S. (2021). Escarpment retreat rates derived from detrital cosmogenic  
 908 nuclide concentrations. *Earth Surface Dynamics Discussions* [preprint], 1-38.  
 909 doi:10.5194/esurf-2021-27
- 910 Wells, N., Andriamihaja, B., Goodman, S., & Patterson, B. (1997). Extreme gully erosion in  
 911 madagascar and its natural and anthropogenic causes. *Natural change and human*  
 912 *impact in Madagascar*, 44-47.
- 913 Wells, N. A., & Andriamihaja, B. (1990). Evidence for cryptic colluvial addition and removal  
 914 at the tops of laterite profiles in madagascar/mise en evidence d'apport et d'ablation de  
 915 colluvions cryptiques au sommet de profils lateritiques de madagascar. *Sciences*  
 916 *Geologiques, bulletins et memoires*, 43 (2), 237-251. doi:10.3406/sgeo;/1990.1858
- 917 Whipple, K. X., & Tucker, G. E. (1999). Dynamics of the stream-power river incision model:  
 918 Implications for height limits of mountain ranges, landscape response timescales, and  
 919 research needs. *Journal of Geophysical Research: Solid Earth*, 104(B8), 17661-17674.  
 920 doi : 10.1029/1999jb900120
- 921 Willett, S. D., McCoy, S. W., & Beeson, H. W. (2018). Transience of the north American  
 922 high plains landscape and its impact on surface water. *Nature*, 561 (7724), 528-532.  
 923 doi:10.1038/s41586-018-0532-1
- 924 Willett, S. D., McCoy, S. W., Perron, J. T., Goren, L., & Chen, C. Y. (2014). Dynamic  
 925 reorganization of river basins. *Science*, 343(6175). doi: 10.1126/science.1248765
- 926 Wit, M. J. d. (2003). Madagascar: heads its a continent, tails its an island. *Annual Review of*  
 927 *Earth and Planetary Sciences*, 31 (1), 213-248.  
 928 doi:10.1146/annurev.earth.31.100901.141337
- 929 Wobus, C., K. X. Whipple, E. Kirby, N. Snyder, J. Johnson, K. Spyropolou, B. Crosby, and  
 930 D. Sheehan (2006), *Tectonics from topography: Procedures, promise, and pitfalls*,  
 931 *Geological Society of America, Special Papers*, 398, 55– 74,  
 932 doi:10.1130/2006.2398(04).  
 933

## **[Retreat of the Great Escarpment of Madagascar from Geomorphic Analysis and Cosmogenic $^{10}\text{Be}$ Concentrations ]**

Y. Wang<sup>1</sup>, S. D. Willett<sup>1</sup>, D. Wu<sup>2</sup>, N. Haghpor<sup>1</sup>, M. Christl<sup>3</sup>

<sup>1</sup>ETH Zurich, Department of Earth Sciences, Sonneggstrasse 5, 8092 Zurich, Switzerland.

<sup>2</sup>China Geological Survey, Shengyang Center, Huanghe North Street 280, 110034 Shenyang, China.

<sup>3</sup>ETH Zurich, Department of Physics, Laboratory of Ion Beam Physics, Otto-Stern-Weg 5, 8093 Zurich, Switzerland.

### **Contents of this file**

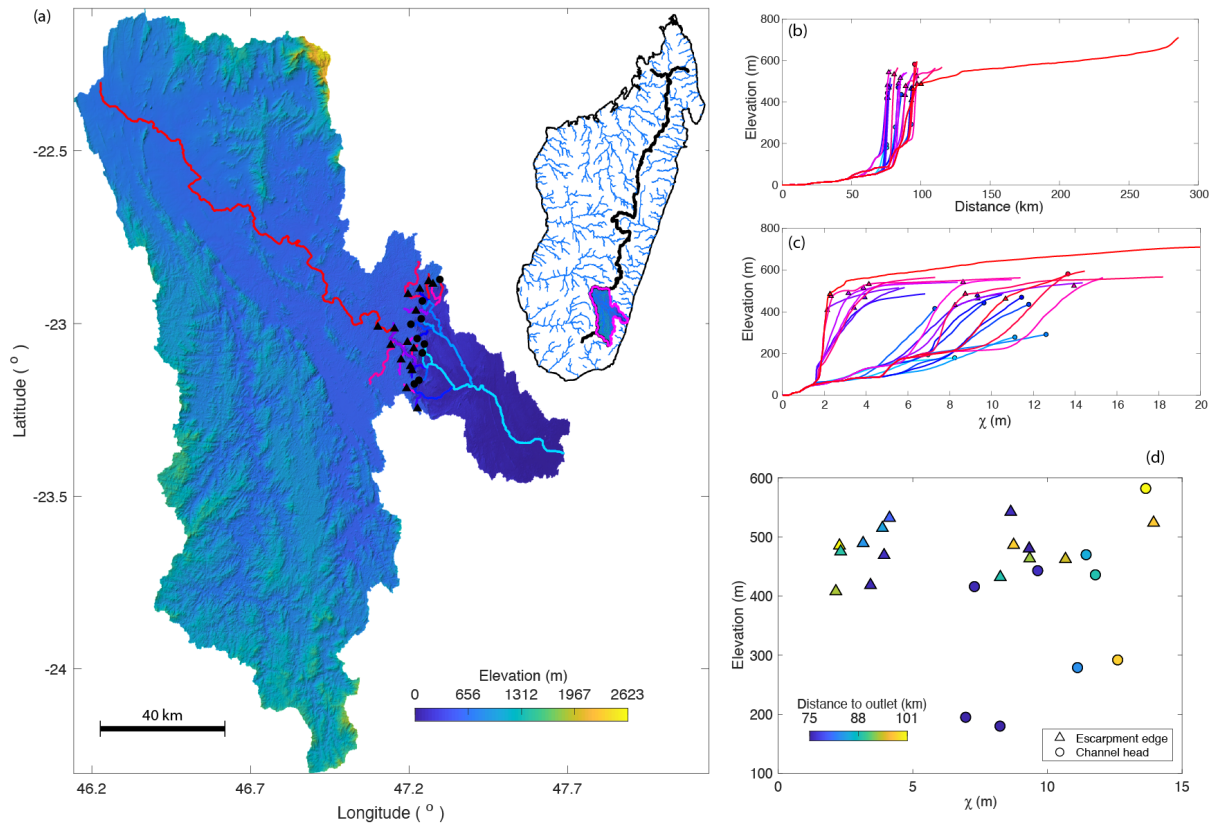
Figures S1 to S5

Tables S1

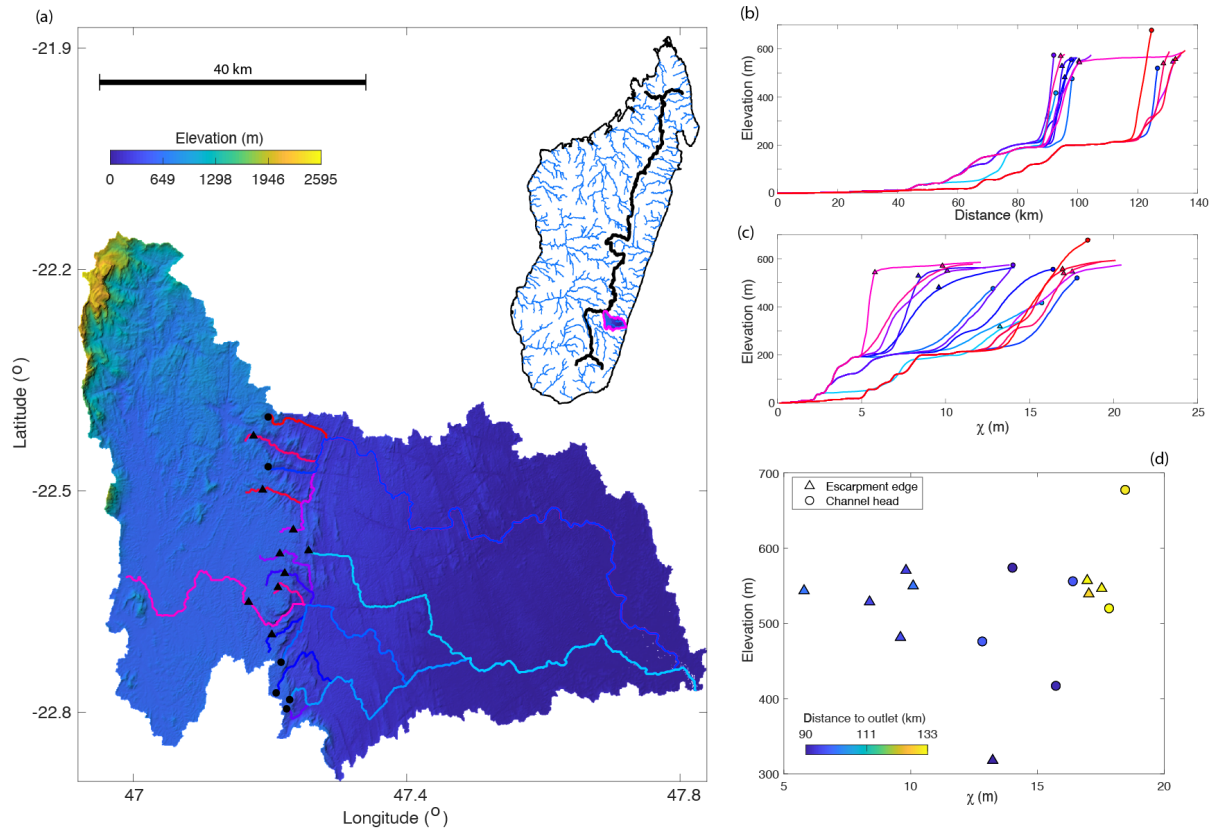
### **Introduction**

Figure S1 to S5 show the morphology of escarpment-draining rivers of major escarpment basins. The transformed  $\chi$  profile is calculated by the integral of river length and normalized for the discharge (Perron and Royden, 2013) as there is a strong orographic effects of precipitation across the escarpment (Scroxtton et al., 2017). Discharge is approximated by the product of drainage area and precipitation.

Table S1 presents escarpment retreat rates of Madagascar and Western Ghats of India that are corrected for various lithospheric rigidities and plateau area.



**Figure S1.** (a) SRTM digital elevation model (Jarvis et al., 2008) of the Mananara River basin in eastern Madagascar. Basin location is indicated in the inset. (b) river profiles, escarpment edges are marked with triangles and channel heads are marked with filled circles (c) transformed  $\chi$ -elevation profiles. (d) Position of the escarpment edge where this is identifiable as a knickzone or the channel head where there is no knickzone.



**Figure S2.** (a) SRTM digital elevation model (Jarvis et al., 2008) of an escarpment-draining basin in eastern Madagascar. Basin location is indicated in the inset. (b) river profiles, escarpment edges are marked with triangles and channel heads are marked with filled circles (c) transformed  $\chi$ -elevation profiles. (d) Position of the escarpment edge where this is identifiable as a knickzone or the channel head where there is no knickzone.

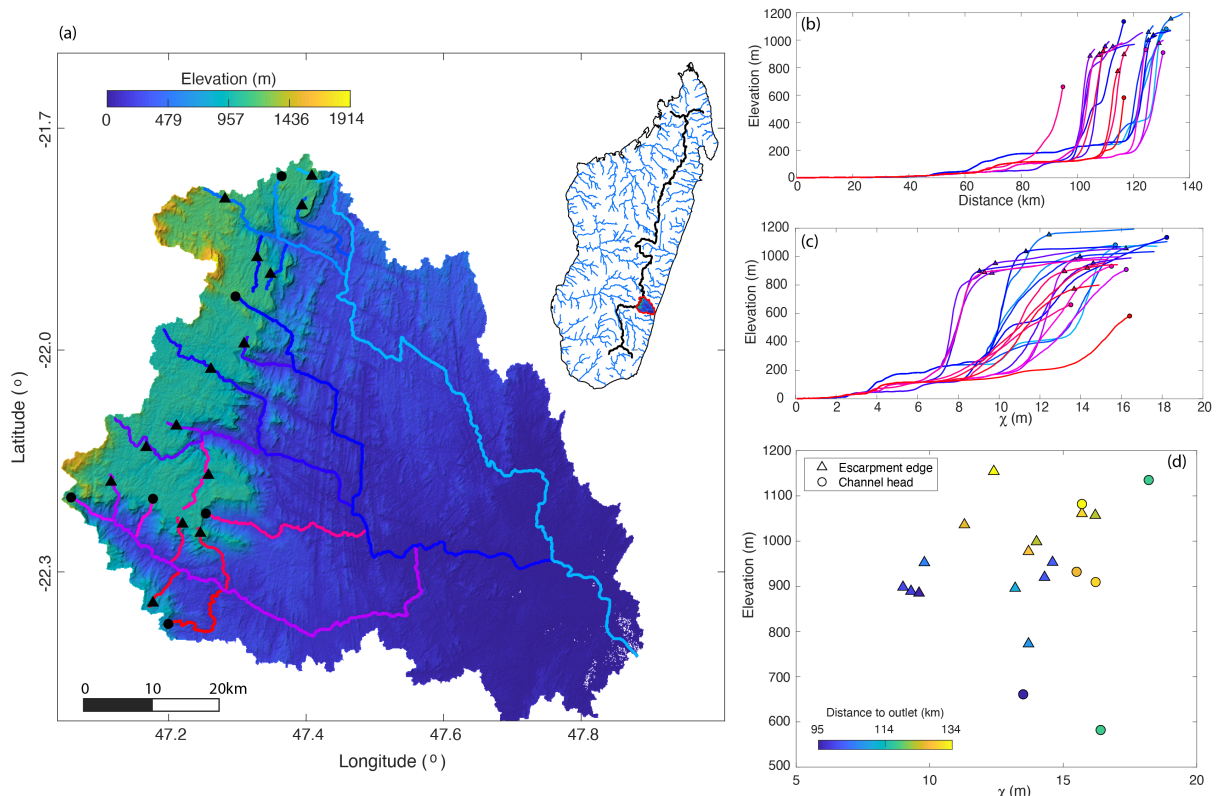


**Figure S3.** (a) SRTM digital elevation model (Jarvis et al., 2008) of an escarpment-draining basin in eastern Madagascar. Basin location is indicated in the inset. (b) river profiles, escarpment edges are marked with triangles and channel heads are marked with filled circles (c) transformed  $\chi$ -elevation profiles. (d) Position of the escarpment edge where this is identifiable as a knickzone or the channel head where there is no knickzone.

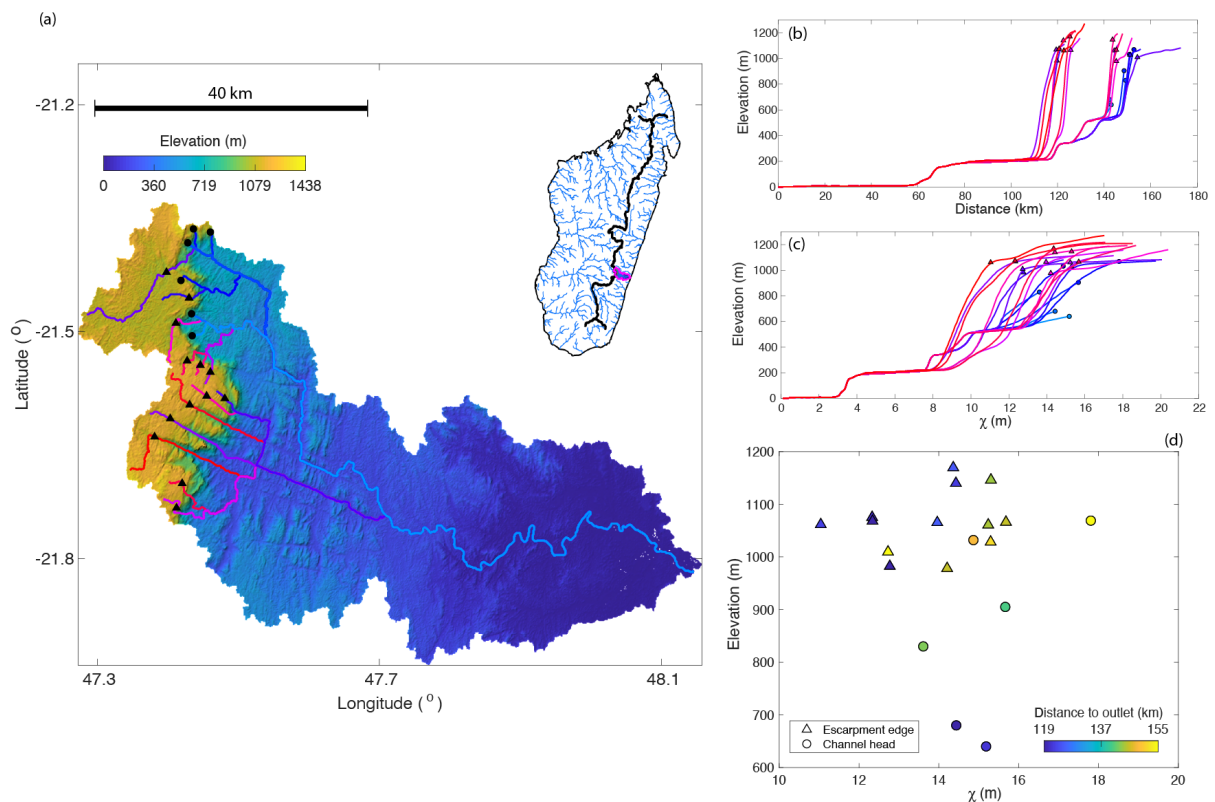


**Figure S4.** (a) SRTM digital elevation model (Jarvis et al., 2008) of an escarpment-draining basin in eastern Madagascar. Basin location is indicated in the inset. (b) river profiles, escarpment edges are marked with triangles and channel heads are marked with filled circles (c) transformed  $\chi$ -elevation profiles. (d) Position of the escarpment edge where this is identifiable as a knickzone or the channel head where there is no knickzone.

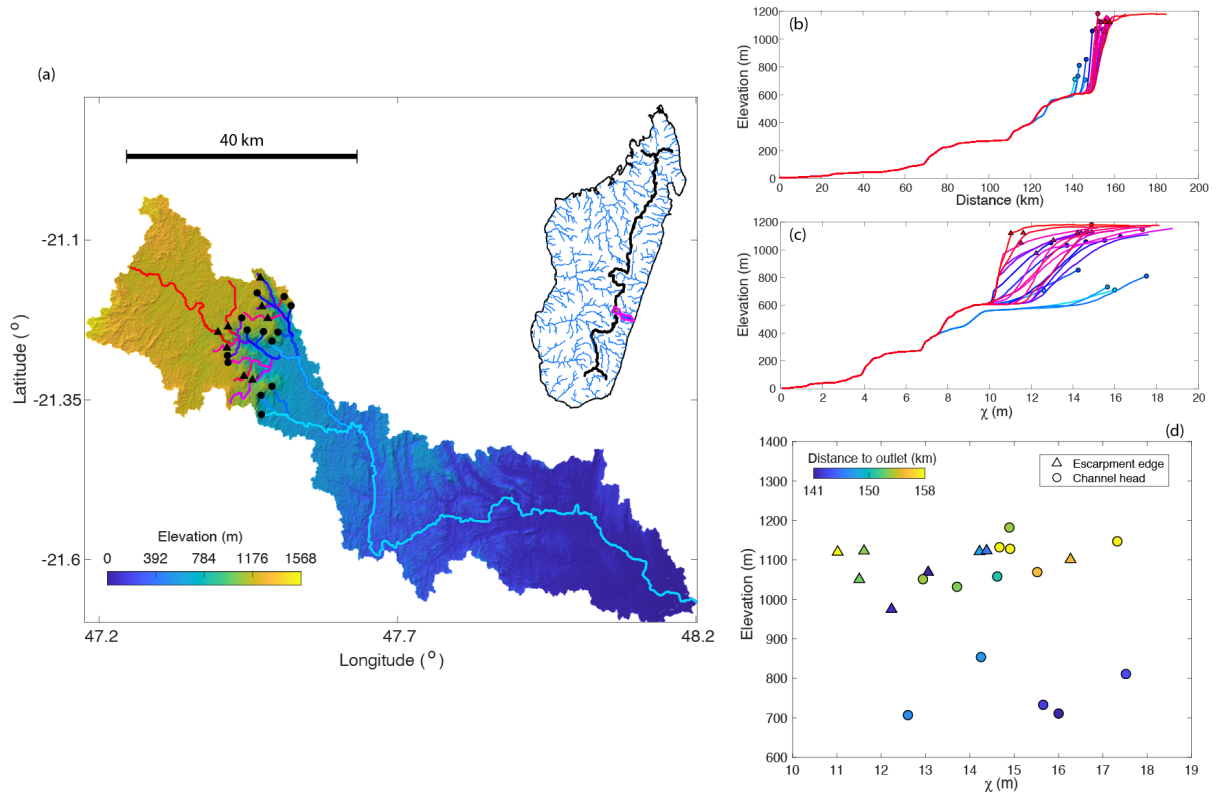


**Figure S5.** (a) SRTM digital elevation model (Jarvis et al., 2008) of an escarpment-draining basin in eastern Madagascar. Basin location is indicated in the inset. (b) river profiles, escarpment edges are marked with triangles and channel heads are marked with filled circles (c) transformed  $\chi$ -elevation profiles. (d) Position of the escarpment edge where this is identifiable as a knickzone or the channel head where there is no knickzone.

Basin	<sup>(a)</sup> Flexural rebound effect $R_A$ (%)			Retreat rate (m/Ma)			<sup>10</sup> Be reference	<sup>(d)</sup> Basin number
	<sup>(b)</sup> Density ratio = 0.85			Corrected for both plateau area and flexural rebound				
	<sup>(c)</sup> $T_e=5\text{km}$	$T_e=10\text{km}$	$T_e=50\text{km}$	$T_e=5\text{km}$	$T_e=10\text{km}$	$T_e=50\text{km}$		
<b>Madagascar</b>								
MDG 1653D2	22.1	13.9	4.3	141	156	173	This study	1
MDG 1631B1	20.2	12.5	3.8	105	115	127	This study	3
MDG 1609A1	27.0	17.3	5.4	195	221	253	This study	4
MDG 1586D1	35.2	24.1	7.9	300	351	426	This study	5
MDG 1610A1	42.7	32.8	11.7	295	346	455	This study	6
MDG 1460C1	17.2	10.6	3.2	341	368	399	This study	7
MDG 1405A1	40.6	29.9	10.3	699	825	1055	This study	9
MDG 1318A2	37.2	26.1	8.7	667	785	970	This study	10
MDG 1287B2	36.3	25.2	8.3	862	1012	1241	This study	11
MDG 1204C1	34.6	23.5	7.7	587	686	828	This study	13
MDG 1147D1	19.1	11.8	3.6	621	677	740	This study	15
MDG 1176C1	39.2	28.2	9.5	821	970	1223	This study	14
MDG 1234D1	43.2	45.3	25.8	1157	1115	1512	This study	12
MDG 1038C1	41.5	31.1	10.9	498	586	758	This study	20
MDG 1122C1	19.1	11.8	3.6	337	367	401	This study	16
<b>Western Ghats, India</b>								
SIN1440	21.1	13.1	4.0	161	177	195	Mandal et al., 2015	1
SIN1380	11.4	6.9	2.1	141	148	155	Mandal et al., 2015	2
SIN1435	8.1	4.8	1.5	177	184	190	Mandal et al., 2015	3
SIN1369	33.1	22.2	7.2	354	411	491	Mandal et al., 2015	4
SIN1368	30.7	20.2	6.4	574	661	775	Mandal et al., 2015	5
SIN1362	38.4	27.4	9.2	752	886	1108	Mandal et al., 2015	6
SIN1361	39.5	28.5	9.7	550	650	821	Mandal et al., 2015	7
SIN1421	4.8	2.9	0.9	307	313	319	Mandal et al., 2015	8
SIN1331	17.0	10.4	3.2	637	687	742	Mandal et al., 2015	9
SIN1332	23.8	15.0	4.7	555	619	694	Mandal et al., 2015	10
SIN1330	25.8	16.4	5.1	477	538	610	Mandal et al., 2015	11
SIN1348	14.7	8.9	2.7	288	308	329	Mandal et al., 2015	12
SIN1379	16.1	9.8	3.0	178	191	206	Mandal et al., 2015	13
SIN1416	6.4	3.8	1.1	244	251	258	Mandal et al., 2015	14
SIN1350	15.3	9.3	2.8	282	302	324	Mandal et al., 2015	15
SIN1351	17.2	10.6	3.2	349	377	408	Mandal et al., 2015	16
SIN1407	7.0	4.2	1.2	178	184	190	Mandal et al., 2015	17
SIN1433	8.9	5.4	1.6	226	235	244	Mandal et al., 2015	18
SIN1432	12.1	7.3	2.2	235	248	262	Mandal et al., 2015	19
SIN1367	30.4	20.0	6.3	327	375	440	Mandal et al., 2015	20
SIN1430	11.2	6.8	2.0	390	410	431	Mandal et al., 2015	21
SIN1427	6.8	4.1	1.2	271	279	288	Mandal et al., 2015	22
SIN1429	23.8	15.0	4.7	267	298	334	Mandal et al., 2015	23
SIN1419	13.1	7.9	2.4	429	455	482	Mandal et al., 2015	24

**Table S1.** Flexural rebound correction for escarpment retreat rates for basins of Madagascar and Western Ghats of India. (a) the ratio of isostatically-uplifted mass removed relative to the retreat mass removal. (b) the density ratio between crust and mantle. (c) the effective elastic thickness of the lithosphere. (d) basin number on Figure 11.

## Reference

- Jarvis, A., Reuter, H., Nelson, A., & Guevara, E. (2008). Hole-filled seamless SRTM data, version 4, international centre for tropical agriculture (ciat). Retrieved from <http://srtm.csi.cgiar.org>
- Mandal, S. K., Lupker, M., Burg, J.-P., Valla, P. G., Haghypour, N., & Christl, M. (2015). Spatial variability of <sup>10</sup>be-derived erosion rates across the southern peninsular indian escarpment: A key to landscape evolution across passive margins. *Earth and Planetary Science Letters*, 425, 154-167. doi:10.1016/j.epsl.2015.05.050
- Perron, J.T. and Royden, L. (2013), An integral approach to bedrock river profile analysis. *Earth Surf. Process. Landforms*, 38: 570-576. doi:10.1002/esp.3302

Scropton, N., Burns, S. J., McGee, D., Hardt, B., Godfrey, L. R., Ranivoharimanana, L., & Faina, P. (2017). Hemispherically in-phase precipitation variability over the last 1700 years in a madagascar speleothem record. *Quaternary Science Reviews*, 164 , 25-36. doi:10.1016/j.quascirev.2017.03.017